PACE Technical Report Series, Volume 6

Ivona Cetinić, Charles R. McClain, and P. Jeremy Werdell, Editors

Data Product Requirements and Error Budgets Consensus Document

Ziauddin Ahmad, Ivona Cetinić, Bryan A. Franz, Erdem M. Karaköylü, Lachlan I. W. McKinna, Frederick S. Patt, and Jeremy Werdell

NASA STI Program ... in Profile

Since its founding, NASA has been dedicated to the advancement of aeronautics and space science. The NASA scientific and technical information (STI) program plays a key part in helping NASA maintain this important role.

The NASA STI program operates under the auspices of the Agency Chief Information Officer. It collects, organizes, provides for archiving, and disseminates NASA's STI. The NASA STI program provides access to the NASA Aeronautics and Space Database and its public interface, the NASA Technical Report Server, thus providing one of the largest collections of aeronautical and space science STI in the world. Results are published in both non-NASA channels and by NASA in the NASA STI Report Series, which includes the following report types:

- TECHNICAL PUBLICATION. Reports of completed research or a major significant phase of research that present the results of NASA Programs and include extensive data or theoretical analysis. Includes compilations of significant scientific and technical data and information deemed to be of continuing reference value. NASA counterpart of peer-reviewed formal professional papers but has less stringent limitations on manuscript length and extent of graphic presentations.

- TECHNICAL MEMORANDUM. Scientific and technical findings that are preliminary or of specialized interest, e.g., quick release reports, working papers, and bibliographies that contain minimal annotation. Does not contain extensive analysis.

- CONTRACTOR REPORT. Scientific and technical findings by NASA-sponsored contractors and grantees.

- CONFERENCE PUBLICATION. Collected papers from scientific and technical conferences, symposia, seminars, or other meetings sponsored or co-sponsored by NASA.

- SPECIAL PUBLICATION. Scientific, technical, or historical information from NASA programs, projects, and missions, often concerned with subjects having substantial public interest.

- TECHNICAL TRANSLATION. English-language translations of foreign scientific and technical material pertinent to NASA's mission.

Specialized services also include organizing and publishing research results, distributing specialized research announcements and feeds, providing help desk and personal search support, and enabling data exchange services. For more information about the NASA STI program, see the following:

- Access the NASA STI program home page at http://www.sti.nasa.gov

- E-mail your question via the Internet to help@sti.nasa.gov

- Phone the NASA STI Information Desk at 757-864-9658

- Write to:
  NASA STI Information Desk
  Mail Stop 148
  NASA's Langley Research Center
  Hampton, VA 23681-2199

NASA/TM–2018-219027/ Vol. 6
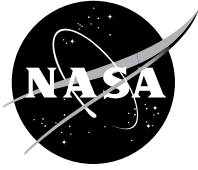
PACE Technical Report Series, Volume 6

Editors:

Ivona Cetinić
GESTAR/Universities Space Research Association, Columbia, Maryland

Charles R. McClain
Science Applications International Corporation, Reston, Virginia

P. Jeremy Werdell
NASA Goddard Space Flight Center, Greenbelt, Maryland

Data Product Requirements and Error Budgets Consensus Document

Ziauddin Ahmad
Science Applications International Corporation, Reston, Virginia

Ivona Cetinić
GESTAR/Universities Space Research Association, Columbia, Maryland

Bryan A. Franz
NASA Goddard Space Flight Center, Greenbelt, Maryland

Erdem M. Karaköylü
Science Applications International Corporation, Reston, Virginia

Lachlan I. W. McKinna
Go2Q Pty, Ltd, Buderim, Australia

Frederick S. Patt
Science Applications International Corporation, Reston, Virginia

Jeremy Werdell
NASA Goddard Space Flight Center, Greenbelt, Maryland

National Aeronautics and
Space Administration

Goddard Space Flight Center
Greenbelt, Maryland 20771

January 2019

INTRODUCTION
Introduction to Volume 6: Data Product Requirements and Error Budgets

The Plankton, Aerosol, Cloud, ocean Ecosystem (PACE; https://pace.gsfc.nasa.gov) mission represents NASA's next great investment in satellite ocean color and the combined study of Earth's ocean-atmosphere system. At its core, PACE builds upon NASA's multi-decadal legacies of the Coastal Zone Color Scanner (1978-1986), Sea-viewing Wide Field-of-view Sensor (SeaWiFS; 1997-2010), Moderate Resolution Imaging Spectroradiometers (MODIS) onboard Terra (1999-present) and Aqua (2002-present), and Visible Infrared Imaging Spectroradiometer (VIIRS) onboard Suomi NPP (2012-present) and JPSS-1 (2017-present; to be renamed NOAA-20). The ongoing, combined climate data record from these instruments changed the way we view our planet and – to this day – offers an unparalleled opportunity to expand our senses into space, compress time, and measure life itself.

This volume presents PACE science data requirements and the studies conducted and tools developed that translate these requirements into performance metrics for the ocean color instrument (OCI). In many ways, these studies and tools became the Rosetta Stone that translated PACE science into OCI engineering. The volume opens with presentation of Level-1 science data product requirements delivered to the PACE mission by NASA HQ. These requirements encompass data products to be produced and their associated uncertainties. The remainder of the volume describes tools developed that allocate these uncertainties into their components, including allowable OCI systematic and random uncertainties, observatory geolocation uncertainties, and geophysical model uncertainties. To the best of our knowledge, many of these tools did not previously exist and, thus, offer new and substantial resources to the ocean color satellite user community.

I offer my thanks to the PACE Project Science team for their ingenuity and resourcefulness in pursing these activities. I also thank the OCI systems engineering team for the frank and honest dialog and their willingness to help bridge the gap between science and engineering. We collectively hope that the user community benefits from – and, perhaps more importantly, builds upon – these efforts.

P. J. Werdell
PACE Project Scientist
March 2018

Contents

Chapter 1

PACE Ocean Color Science Data Product Requirements

Jeremy Werdell, NASA Goddard Space Flight Center, Greenbelt, Maryland[1]

Executive Summary

This chapter summarizes ocean color science data product requirements for the Plankton, Aerosol, Cloud, ocean Ecosystem (PACE) mission's Ocean Color Instrument (OCI) and observatory. NASA HQ delivered Level-1 science data product requirements to the PACE Project, which encompass data products to be produced and their associated uncertainties. These products and uncertainties ultimately determine the spectral nature of OCI and the performance requirements assigned to OCI and the observatory. This chapter ultimately serves to provide context for the remainder of this volume, which describes tools developed that allocate these uncertainties into their components, including allowable OCI systematic and random uncertainties, observatory geolocation uncertainties, and geophysical model uncertainties.

1.1.   Introduction

Core science objectives of any satellite mission depend primarily on the quality of science data products delivered by the instrument payload. In May 2015, NASA HQ Earth Science Division (ESD) delivered threshold Level-1 requirements to the Plankton, Aerosol, Cloud, ocean Ecosystem (PACE) Project, which included a list of science data products to be produced, along with their associated uncertainties. These products encompass ocean color, aerosol, and cloud retrievals and represent the core suite of measurements required to achieve PACE mission science objectives. As the Ocean Color Instrument (OCI) remains the only required instrument on the mission observatory, it alone must be capable of producing all science data products. Following, the suite of required science data products ultimately drives the OCI design concept and all performance requirements for OCI and the PACE observatory.

Within a flight project, a series of flowed-down requirements translate science into engineering. For PACE, Level-1 requirements are managed by NASA ESD, Level-2 requirements (subordinate, more detailed requirements necessary to meet Level-1 requirements) are derived and managed by the PACE Project, and Level-3 requirements (subordinate, more detailed requirements necessary to meet Level-2 requirements) are derived and managed by specific Project elements, such as the OCI systems engineering team. This volume presents analyses and tools developed by the PACE Project Science team to derive Level-2 performance requirements from the ESD-provided Level-1 science data products requirements (Figure 1.1).

NASA flight projects also typically carry two versions of requirements at each level, at least for Level-1 requirements. *Threshold* requirements indicate the minimum suite necessary to proceed with the mission. *Baseline* requirements describe those above-and-beyond threshold that a project expects to achieve. In practice, instruments systems engineering teams pursue design concepts that meet or exceed baseline requirements. For PACE, threshold requirements are set by NASA HQ and remain unchanged,

---

whereas baseline requirements will not be finalized until Key Decision Point C (KDP-C, scheduled for June 2019 at the time of this writing). Under the auspices of Design-to-Cost (see Volume 3 in this Technical Memorandum series), baseline requirements remain in mission trade space until mission confirmation at KDP-C.

```
                    ┌──────────────────┐
                    │     Level 1      │
                    │   Measurement    │
                    │   Uncertainty    │
                    └──────────────────┘
         ┌───────────────────┼───────────────────┐
┌────────────────┐  ┌────────────────┐  ┌────────────────┐
│    Level 2     │  │    Level 2     │  │    Level 2     │
│   Systematic   │  │     Random     │  │      SDS       │
│   Uncertainty  │  │   Uncertainty  │  │   Uncertainty  │
└────────────────┘  └────────────────┘  └────────────────┘
```
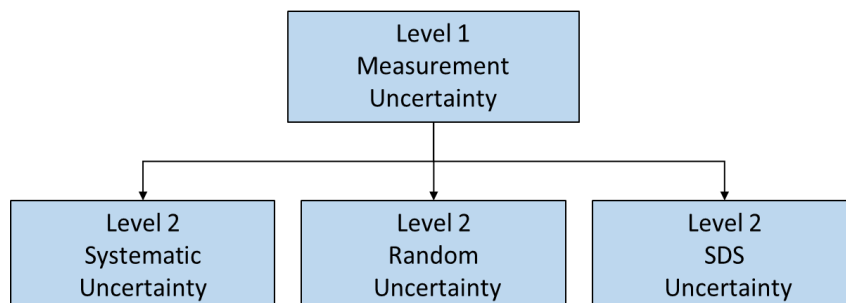
Figure 1.1. Requirement sub-allocations from Level-1 measurements uncertainties into Level-2 component uncertainties. Chapters in this volume describe methods used to derive each Level-2 allocation. SDS indicates Science Data Segment and represents uncertainties associated with atmospheric correction and other post-launch components of the mission.

The remainder of this chapter is dedicated to presenting Level-1 threshold and baseline ocean color science data products requirements for PACE's OCI and example Level-2 sub-allocations of data product uncertainties, which will be presented in detail in the remainder of this volume. Level-1 requirements for aerosol and cloud products are also presented, but are not explored in detail at this time as the ocean color retrieval requirements dominate the derivation of performance specifications for OCI. Volume 5 of this Technical Report series includes additional details on OCI capabilities for aerosol and cloud retrievals.

1.2.   Level-1 Requirements

Threshold and baseline requirements for ocean color data products are as follows:

Data Product	Threshold Uncertainty	Baseline Uncertainty
Water-leaving reflectances centered on (±2.5 nm) 350, 360, and 385 nm (15 nm bandwidth)	0.0083 or 30%	0.0057 or 20%
Water-leaving reflectances centered on (±2.5 nm) 412, 425, 443, 460, 475, 490, 510, 532, 555, and 583 (15 nm bandwidth)	0.0024 or 6%	0.0020 or 5%
Water-leaving reflectances centered on (±2.5 nm) 617, 640, 655, 665, 678, and 710 (15 nm bandwidth, except for 10 nm bandwidth for 665 and 678 nm)	0.00084 or 12%	0.0007 or 10%
Ocean Color Data Products to be Derived from Water-leaving Reflectances		
Concentration of chlorophyll-a (mg m^{-3})		
Diffuse attenuation coefficients from 400-600 nm (m^{-1})		
Phytoplankton absorption from 400-600 nm (m^{-1})		
Non-algal particle plus dissolved organic matter absorption from 400-600 nm (m^{-1})		

Particle backscattering from 400-600 nm (m^{-1})	
Fluorescence line height (mW cm^{-2} μm^{-1} sr^{-1})	

Each uncertainty requirement is defined by the greater of the absolute and relative value and for 50% or more of the observable deep ocean (depth>1000 m) at a Level-2 satellite data processing level (Figure 1.2; geophysical values without spatial or temporal re-projection and compositing). Only water-leaving reflectances (unitless) carry uncertainties. Note also that the PACE mission will provide a suite of oceanographic geophysical variables beyond those listed above, including, but not limited to, carbon stocks and fluxes, photosynthetic pigment concentrations, and indices of phytoplankton community composition and health.

Threshold and baseline aerosol and cloud products are identical as follows:

Data Product	Range	Uncertainty
Total aerosol optical depth at 380 nm	0.05 to 5	0.06 or 40%
Total aerosol optical depth at 440, 500, 550 and 675 nm over land	0.05 to 5	0.06 or 20%
Total aerosol optical depth at 440, 500, 550 and 675 nm over oceans	0.05 to 5	0.04 or 15%
Fraction of visible aerosol optical depth from fine mode aerosols over oceans at 550 nm	0.05 to 1	±25%
Cloud layer detection for optical depth < 0.3	Not defined	40%
Cloud top pressure of opaque (optical depth > 3) clouds	100 to 1000 hPa	60 hPa
Optical thickness of liquid clouds	5 to 100	25%
Optical thickness of ice clouds	5 to 100	35%
Effective radius of liquid clouds	5 to 50 μm	25%
Effective radius of ice clouds	5 to 50 μm	35%
Atmospheric data products to be derived from the above		
Water path of liquid clouds		
Water path of ice clouds		
Shortwave radiation effect		

Each uncertainty requirement is defined by the greater of the absolute and relative value and for 65% or more of the observable atmosphere at a Level-2 satellite data processing level (Figure 1.2) for all products except shortwave radiation effect. The shortwave radiation effect is for a seasonal, hemispheric average since that is the temporal/spatial domain over which it can be validated against other sensors/observational networks.

Ultimately, the Project – in particular, the Project Science team – remains responsible for ensuring the PACE's OCI can produce these geophysical data products at the prescribed uncertainty levels, which requires both a high-performance OCI and a validation program. With regards to the former, the Project Science team works closely with the OCI systems engineering team to translate science requirements into engineering requirements and design an OCI concept that can adequately produce these geophysical variables. The first step in this is development of tools that allocate total uncertainties into instrument and geophysical model performance specifications, which become Level-2 requirements (and, can be subsequently used to verify instrument performance during its development, testing, and observatory integration).

1.3. Level-2 Requirements

Following Figure 1.1, total uncertainty, σ_{total}, is defined as the root sum square of geophysical algorithm (model), systematic, and random errors:

$$\sigma_{total} = \sqrt{\sigma_{systematic}^2 + \sigma_{random}^2 + \sigma_{model}^2}$$ (Eq. 1.1)

An example of how total baseline uncertainties might be allocated for ocean color Level-1 requirements is as follows:

Data Product	Systematic Error	Random Error	Model Error
Water-leaving reflectances centered on (±2.5 nm) 350, 360, and 385 nm (15 nm bandwidth)	0.0055	0.0.008	0.0008
Water-leaving reflectances centered on (±2.5 nm) 412, 425, 443, 460, 475, 490, 510, 532, 555, and 583 (15 nm bandwidth)	0.0018	0.0006	0.0005
Water-leaving reflectances centered on (±2.5 nm) 617, 640, 655, 665, 678, and 710 (15 nm bandwidth, except for 10 nm bandwidth for 665 and 678 nm)	0.0005	0.0003	0.0003

Similarly, total threshold uncertainties might be allocated as follows:

Data Product	Systematic Error	Random Error	Model Error
Water-leaving reflectances centered on (±2.5 nm) 350, 360, and 385 nm (15 nm bandwidth)	0.0082	0.0.010	0.0008
Water-leaving reflectances centered on (±2.5 nm) 412, 425, 443, 460, 475, 490, 510, 532, 555, and 583 (15 nm bandwidth)	0.0022	0.0007	0.0005
Water-leaving reflectances centered on (±2.5 nm) 617, 640, 655, 665, 678, and 710 (15 nm bandwidth, except for 10 nm bandwidth for 665 and 678 nm)	0.0007	0.00035	0.0003

Detailed discussions on defining and deriving systematic, random, and model errors appear in Chapter 3, 4, and 6 of this volume [*Ahmad and Franz*, 2018; *Franz and Karaköylü*, 2018; *Patt*, 2018]. Briefly, for PACE, systematic errors refer to image artifacts and biases, such as radiometric stability, temperature sensitivity, polarization, crosstalk, geolocation pointing knowledge, linearity, and response-versus-scan angle, among others (Figure 1.2). Random errors flow to OCI as a uniform scene SNR requirement. Model errors encompass atmospheric correction (that is, derivation of water-leaving reflectances, the Level-1 required data product) from calibrated, geolocated top-of-atmosphere radiances collected by OCI.
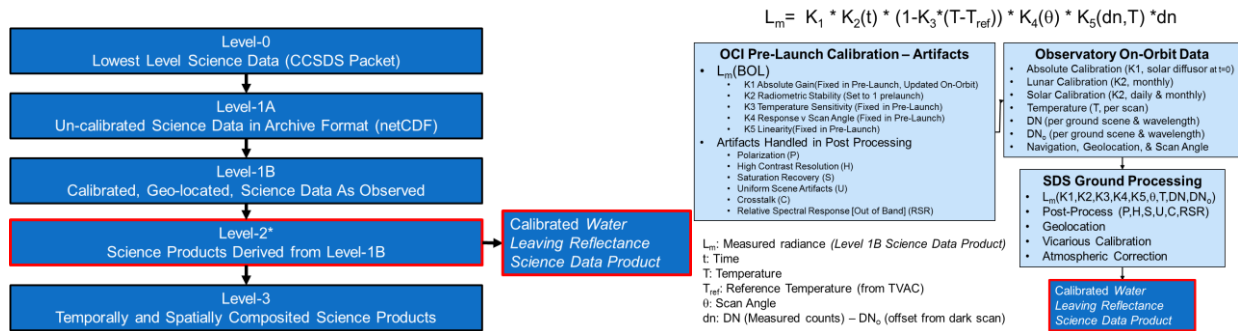
$$L_m = K_1 * K_2(t) * (1-K_3*(T-T_{ref})) * K_4(\theta) * K_5(dn,T) *dn$$

Level-0
Lowest Level Science Data (CCSDS Packet)

Level-1A
Un-calibrated Science Data in Archive Format (netCDF)

Level-1B
Calibrated, Geo-located, Science Data As Observed

Level-2*
Science Products Derived from Level-1B

Level-3
Temporally and Spatially Composited Science Products

Calibrated *Water Leaving Reflectance Science Data Product*

OCI Pre-Launch Calibration – Artifacts
- L_m(BOL)
  - K1 Absolute Gain(Fixed in Pre-Launch, Updated On-Orbit)
  - K2 Radiometric Stability (Set to 1 prelaunch)
  - K3 Temperature Sensitivity (Fixed in Pre-Launch)
  - K4 Response v Scan Angle (Fixed in Pre-Launch)
  - K5 Linearity(Fixed in Pre-Launch)
- Artifacts Handled in Post Processing
  - Polarization (P)
  - High Contrast Resolution (H)
  - Saturation Recovery (S)
  - Uniform Scene Artifacts (U)
  - Crosstalk (C)
  - Relative Spectral Response [Out of Band] (RSR)

L_m: Measured radiance *(Level 1B Science Data Product)*
t: Time
T: Temperature
T_{ref}: Reference Temperature (from TVAC)
θ: Scan Angle
dn: DN (Measured counts) – DN_o (offset from dark scan)

Observatory On-Orbit Data
- Absolute Calibration (K1, solar diffusor at t=0)
- Lunar Calibration (K2, monthly)
- Solar Calibration (K2, daily & monthly)
- Temperature (T, per scan)
- DN (per ground scene & wavelength)
- DN_o (per ground scene & wavelength)
- Navigation, Geolocation, & Scan Angle

SDS Ground Processing
- L_m(K1,K2,K3,K4,K5,θ,T,DN,DN_o)
- Post-Process (P,H,S,U,C,RSR)
- Geolocation
- Vicarious Calibration
- Atmospheric Correction

Calibrated *Water Leaving Reflectance Science Data Product*

Figure 1.2: Science data processing levels (left) and a description of OCI systematic errors.

1.4. Impacts on Geophysical Data Products

The PACE Project expects the final OCI to produce water-leaving reflectances that fall near the baseline requirements, and no worse than the threshold requirements. The following provides an example of how this range of reflectances translates into geophysical data products:

Data Product	Threshold Uncertainty	Baseline Uncertainty
Total absorption at 443-nm	35%	25%
Phytoplankton absorption at 443-nm	35%	25%
Non-algal particle plus dissolved organic matter absorption at 443-nm	35%	20%
Particle backscattering at 443-nm	25%	20%

Chapter 5 of this volume provides the derivation of these uncertainties[*McKinna and Cetinić*, 2018]. These optical properties were derived from water-leaving reflectances using the Generalized Inherent Optical Property (GIOP) framework [*Werdell et al.*, 2013a], as modified in *Werdell et al.* [2013b] and *McKinna et al.* [2016].

1.5. Concluding Remarks

Mission science requirements get translated into engineering and instrument requirements through progressive sub-allocation of allowable uncertainties. This chapter presents Level-1 science data product requirements for the PACE mission (managed by NASA ESD) and describes their flow to Level-2 allocations (managed by the PACE Project at Goddard Space Flight Center), which begin to define OCI performance specifications. Sub-elements of the Project ultimate derive Level-3 (and beyond) requirements from the Level-2's, which ultimately translate into engineering practice and the final OCI design concept. The remainder of this volume describes the definition and derivation of the Level-2 uncertainty sub-allocations.

Chapter 2

Development of PACE OCI Pointing Knowledge and Control Requirements for Geolocation

Frederick S. Patt, Science Applications International Corporation, Reston, Virginia [2]

Executive Summary

The Phytoplankton, Aerosol, Cloud, ocean Ecosystem (PACE) Ocean Color Instrument (OCI) science data product quality depends in part on the accuracy of the spacecraft and instrument pointing knowledge and control. The quality of the geolocation processing performed by the Science Data Segment (SDS) depends primarily on the accuracy of the pointing knowledge. The pointing control and stability can significantly affect the radiometric accuracy and integrity of the science data. The instrument calibration results also depend on accurate pointing control and knowledge. This chapter describes the development of each of these requirements.

2.1. Introduction

Geolocation, the determination of viewed locations, is a key processing step for Earth remote sensing instruments. For satellite-based sensors, geolocation entails three steps: (1) determination of the satellite position in its orbit; (2) determination of the sensor viewing direction, or pointing, using the satellite and sensor orientation information with the sensor geometric model; and, (3) combining these results with a model of the Earth's surface to determine the viewed locations. Heritage missions such as the Sea-viewing Wide Field-of-view Sensor (SeaWiFS) and Moderate-resolution Imaging Spectroradiometer (MODIS) relied upon accurate orbit and pointing knowledge determination to enable geolocation requirements to be met by forward-stream processing [e.g. *Nishihama et al.*, 1997] and automated methods of geolocation assessment to verify requirements and refine the processing methods [*Patt*, 2011; *Wolfe et al.*, 2011].

With the wide availability of accurate orbit data from onboard Global Positioning System (GPS) receivers, determination of the sensor pointing (#2) is subject to the largest errors by far and, hence, is the primary focus of the geolocation error budget for the OCI. Uncertainty in the sensor pointing is the result of contributions from both the OCI and the spacecraft attitude determination and control system (ADCS). The requirements described in this document apply to the combined errors from both sources.

The OCI and spacecraft pointing also affect the quality of the calibration results from the solar and lunar calibrations. The lunar calibration pointing requirements are described in the lunar calibration chapter of Vol.7 PACE TM series [*Patt and Eplee*, 2018]. The following sections present the specific pointing requirements for geolocation and solar calibration, including the justification for each

---

[2] Cite as: Patt, F. (2018), Development of PACE OCI Pointing Knowledge and Control Requirements for Geolocation, in *PACE Technical Report Series, Volume 6: Data Product Requirements and Error Budgets (NASA/TM-2018 – 2018-219027/ Vol. 6)*, edited by I. Cetinić, C. R. McClain and P. J. Werdell, NASA Goddard Space Flight Space Center Greenbelt, MD.

requirement. The PACE Mission Systems Engineering organization has developed and maintained complete error budgets corresponding to the pointing requirements.

2.2. Geolocation Pointing Requirements

The primary drivers for the image geolocation requirements are as follows (see also the PACE Science Definition Team (SDT) report [2018]). Accurate data geolocation is required to enable processing in coastal, as well as open ocean, regions. Specifically, the viewed locations must be known to a fraction of a pixel to enable the effects of coastlines on the nearby measurements to be accurately estimated.

Accurate geolocation is also required to support match-ups with *in situ* and ground (e.g., vicarious) calibration measurements. Since these measurements are point source observations taken at the surface, sub-pixel accuracy of the satellite-based measurements is again needed to ensure accurate match-ups, particularly in highly dynamic or patchy regions of interest.

The overall pointing knowledge requirement encompasses contributions from all sources, including spacecraft attitude determination, sensor alignment, and sensor viewing geometry, and includes static, dynamic, and random terms. The spatial and temporal consistency of measurements is required across all bands to support retrieval algorithms.

The stability requirement for sensor pointing is necessary to maintain image coherency (e.g., scan-to-scan for scanning sensors) for users of swath-based images, and also to support instrumental corrections requiring extended measurement fields, such as for stray light. Finally, although the primary requirements are based on ocean measurements, the potential uses of PACE data by non-ocean (e.g., land) communities support stringent goals in this area.

2.2.1. Pointing Knowledge

The SDT report stated a geolocation knowledge requirement of 0.1 IFOV (1 σ) in each axis, meaning that 68% of all data will have geolocation knowledge errors not exceeding this value. 1-σ errors are generally considered to be equivalent to the root-mean-square of the observed errors. This is equivalent to 92 arcseconds (3 σ) of pointing knowledge uncertainty per axis, with all sources included (spacecraft and OCI). The primary drivers are match-ups to vicarious calibration and *in situ* validation measurements and identification of data affected by coastlines. The match-up requirements impose an absolute upper limit of 0.5 IFOV (3 σ) to ensure that the measurements are associated with the correct OCI observation. This is equivalent to 153 arcseconds of pointing knowledge uncertainty. The accuracy of global coastline databases (e.g., the Global Self-consistent, Hierarchical, High-resolution Shoreline Database, http://www.earthmodels.org/data-and-tools/coastlines/gshhs) is ~100 meters, equivalent to 0.1 IFOV at nadir.

2.2.2. Pointing Control

Pointing control error is the instantaneous difference between the target, or desired, and actual pointing. The target for PACE is specified as the geodetic reference frame at the spacecraft orbit position. Superimposed on this is the instrument tilt of 20 degrees forward or aft.

The pointing control requirement is 2 IFOV (3 σ), equivalent to 613 arcseconds. The primary justification is to minimize variations in geometric viewing angles that would increase the uncertainty in the atmospheric correction. Although this does not impose a hard limit on the pointing control, the requirement can be met by the ADCS and OCI without undue effort.

2.2.3. Pointing Stability

Pointing stability includes variability in the sensor pointing on various time scales, specifically sub-pixel, within a scan, scan-to-scan, and over multiple scans. This makes both the statements of and justifications for the requirements more complicated than for knowledge and control; the requirements need to include both the frequency range and allowable amplitude. Pointing instability is also referred to as jitter. Typical sources of high-frequency jitter are vibration from motor-driven devices such as reaction wheels, while low-frequency sources include other mechanisms (e.g., solar array drive) and the attitude control update frequency

Sub-pixel instability results in blurring of the pixels. The frequency range is determined by the effective integration time. The OCI 1 km pixels have an integration time of ~40 μsec, corresponding to a frequency range of 25 kHz and above. The required amplitude within this range is <30 arcseconds (3 σ); this corresponds to blurring of ~30 m at the 1-σ level.

Instability within a scan and scan-to-scan can result in gaps between scans. The frequency range is from 1 Hz to 25 kHz (the lower limit of the subpixel range). Instability within this range will be a combination of random and systematic effects. The random effects will mainly result from the ADCS control stability on time scales less than 1 second. Systematic effects will result primarily from the instrument, specifically the half-angle mirror (HAM) misalignment to its rotation axis, which will cause alternating gaps and overlaps between successive scans.

The OCI optical design results in a minimum scan overlap of 20 m near the center of the scan and at the minimum PACE orbital altitude (676.5 km over the equator). The stability requirement within this range is 18 arcseconds (3 σ), corresponding to 60 m at scan center. The justification is that 1-σ instability will result in variability of 20 m in the scan-to-scan distance, and therefore no gaps between scans. Figure 2.1 shows an example of a series of scans with random ADCS errors of 30 arcseconds (1 σ) in all three axes, while Figure 2.2 shows an example of HAM misalignment resulting in 30 arcsecond forward and aft pointing errors on alternate scans, both for pixels near scan center. The amplitudes have been intentionally set larger than the requirements to illustrate the effects.

The long-period stability requirement applies to periods of 1 second and longer. This is driven by the need for radiometric accuracy in feature-rich regions of the ocean. To analyze this requirement, an image collected by the Hyperspectral Imager for the Coastal Ocean (HICO) on the International Space Station over the Gulf of Arabia was analyzed to determine the contrast and spatial scale of features. The data at 444 nm was resampled from the HICO native resolution of 90 meters to the OCI resolution of 1 km. Figure 2.3 shows a sample of the data from the scene at both resolutions. The figure shows feature contrast of up to 100% on scales of 5 to 10 km. Based on this, the pointing stability requirement has been specified to maintain areal coverage rates within 3% (3 σ). The requirement is 54 arcseconds/second (3 σ) over periods of 1 second or longer. The justification is the need to maintain areal coverage rates within 3% (3 σ) over regions with high feature contrast.

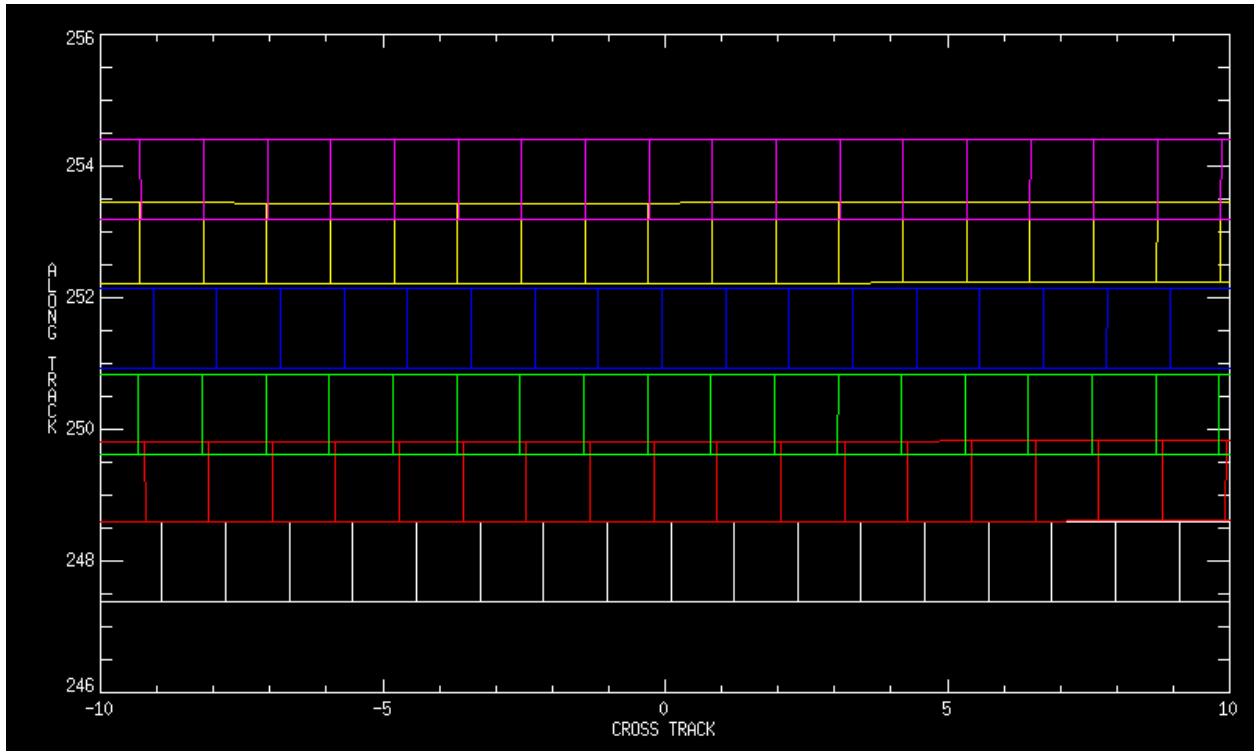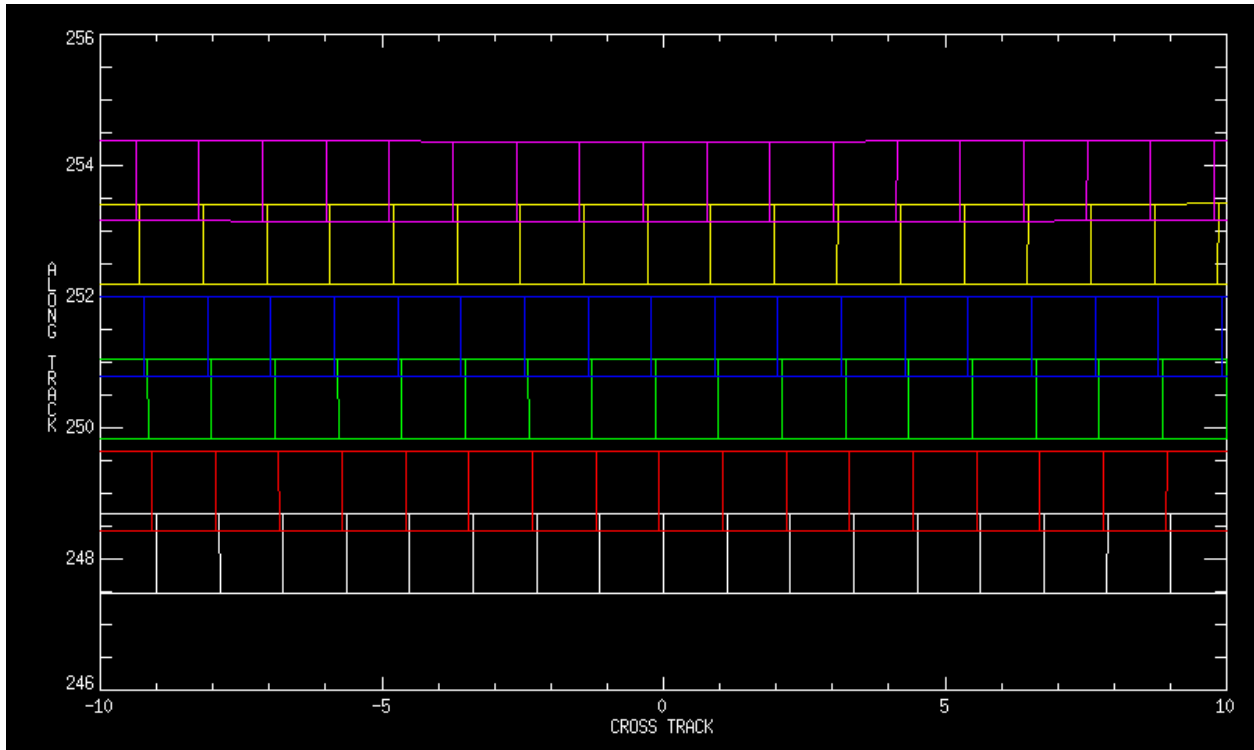*Figure 2.1. Effects of random ADCS pointing errors.*

Figure 2.2. Results of HAM misalignment causing scan-to-scan pointing errors.
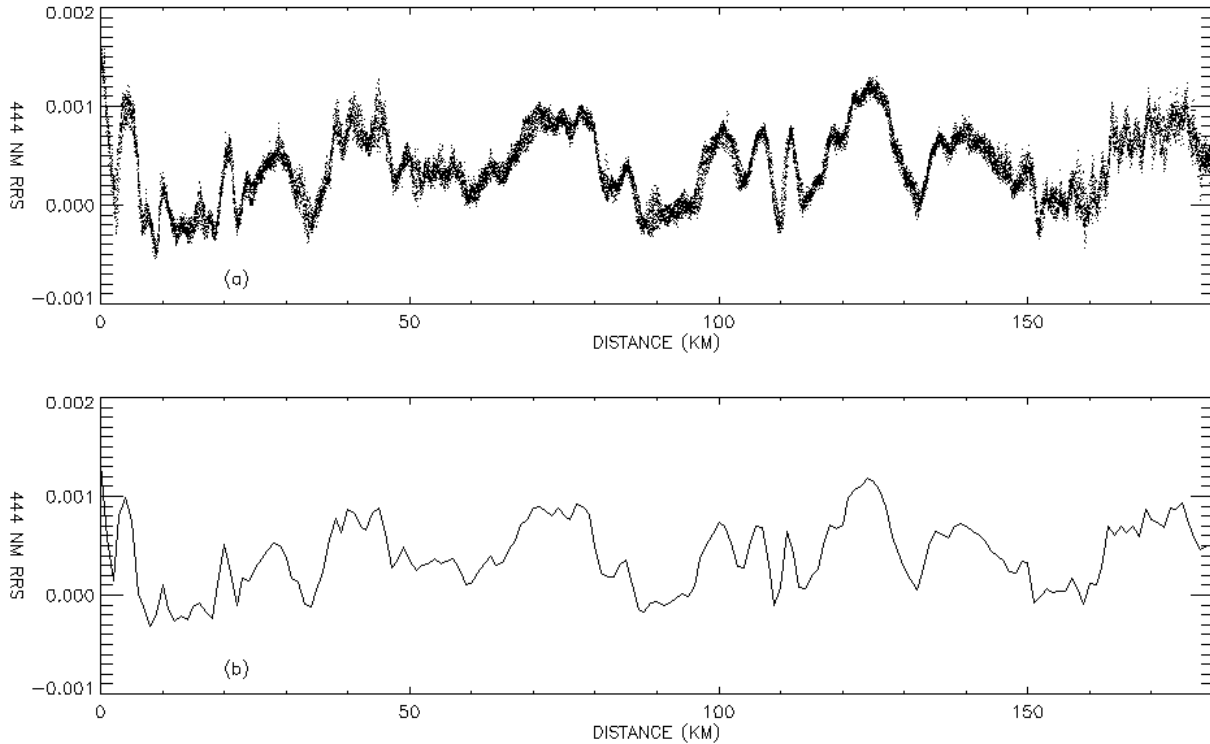
9

Figure 2.3. HICO scene over the Gulf of Arabia showing high contrast features at 444 nm: a) full resolution; b) resampled to 1 km resolution.

2.3. Solar Calibration Pointing Requirements

The pointing requirements for the OCI solar calibration are driven by the need to accurately determine the illumination of the solar diffuser by the Sun. This is directly dependent on the accuracy of the angle of incidence (AOI) of the Sun on the diffuser. The radiance observed by OCI on the diffuser is determined by the solar and instrument AOIs using the bi-directional distribution function (BRDF). The AOI of the instrument line of sight on the diffuser is assumed to be constant for all solar calibration measurements and, therefore, does not contribute to the calibration uncertainty.

As for geolocation, the solar calibration has both control and knowledge requirements for pointing. There is not a separate stability requirement, as long as the knowledge requirement can be maintained over the period of the solar calibration measurement which will be ~TBD seconds for OCI.

Unlike heritage sensors, the OCI solar calibration will be performed with the spacecraft in an inertial pointing mode, to maintain the solar AOI on the diffuser within a small range. The inertial attitude will be determined for each daily solar calibration to achieve the same AOI. The target AOI is 52 degrees.

The pointing control requirement is 0.2 degree (3 σ). The justification is to maintain the solar AOI on the diffuser within a sufficiently small range to allow linear interpolation of the BRDF, in order to minimize the effect of uncertainty in the BRDF on the calibration. Note that this requirement is 720 arcseconds, somewhat less stringent than the corresponding requirement for geolocation.

The pointing knowledge requirement is TBR arcseconds (3 σ). This is also to minimize the BRDF uncertainty, as uncertainty in the pointing knowledge equates directly to uncertainty in the solar AOI. Although this requirement is more stringent than for geolocation, a number of terms in the geolocation pointing knowledge error budget – specifically telescope and HAM – do not contribute to the uncertainty in the solar calibration pointing knowledge.

2.4.   Conclusions

The pointing requirements have been developed for the PACE mission, with the drivers being the OCI science data product quality. Requirements have been developed for pointing control, knowledge and stability. For the last, stability requirements have been developed for a range of frequencies/time periods. In addition, pointing requirements have also been developed for the solar calibration. The requirements are summarized in Table 2.1.

Table 2.1. Pointing requirements

Description	Requirement (3 σ)
Pointing Knowledge	92 arcseconds
Pointing Control	613 arcseconds
Sub-scan Stability	30 arcseconds
Scan-to-scan Stability	18 arcseconds
Long-term Stability	54 arcseconds/second
Solar Calibration Pointing Knowledge	TBR
Solar Calibration Pointing Control	720 arcseconds

Chapter 3

PACE OCI Signal to Noise Performance Requirement: Assessment and Verification Approach for Ocean Color Science

Bryan A. Franz, NASA Goddard Space Flight Center, Greenbelt, Maryland[3]

Erdem M. Karaköylü, Science Applications International Corporation, Reston, Virginia

Executive Summary

This document describes the approach used to determine the Level-2 signal-to-noise (SNR) performance required by the Ocean Color Imager (OCI) on PACE to meet the specified Level-1 uncertainty requirements on the water-leaving reflectance products. Specifically, it is the requirement on the random component of water-leaving reflectance uncertainty that drives the SNR requirements for the OCI instrument in the visible-to-near-infrared (NIR) spectral range (400-900nm). A method is described based on Monte Carlo simulations, which quantifies the spectral water-leaving reflectance uncertainty for a given OCI SNR spectral profile. The method is applied iteratively to find a viable SNR profile that meets the science requirements on allowable random error in water-leaving reflectance, while considering the capabilities and limitations of the OCI instrument design.

3.1. Introduction

With OCI, we seek to measure the spectral distribution of water-leaving radiance or associated water-leaving reflectance ($\rho_w(\lambda)$; dimensionless) in the visible spectral domain (λ), from which the optical properties and constituent concentrations within the water column can be derived. OCI, however, will observe the radiance, $Lt(\lambda)$, exiting the top of Earth's atmosphere (TOA), and an atmospheric correction (AC) algorithm must be applied to retrieve $\rho_w(\lambda)$ from the dominant atmospheric scattering contributions and light reflected from the ocean surface. A primary driver of $\rho_w(\lambda)$ uncertainty is the inherent instrument noise, which propagates through the atmospheric correction process with complex influences across spectral bands and varying atmospheric and water optical properties and radiant path geometries. Given instrument noise as a function of signal in each spectral band, we assess the influence of instrument noise on random error in $\rho_w(\lambda)$ retrieval through a Monte Carlo Analysis (MCA). In the MCA, a representative global dataset of spectral TOA radiances is processed through the AC algorithm many times, but in each iteration, we add random noise to the TOA radiances in each pixel based on the known or expected instrument signal to noise (SNR) model. For each pixel, for each spectral band, the many iterations of $\rho_w(\lambda)$ are then analyzed to determine the retrieval precision that can be expected, given the input noise and the AC algorithm employed.

---

[3] Cite as: Franz, B. A., & Karaköylü, E. M. (2018). PACE OCI Signal to Noise Performance Requirement: Assessment and Verification Approach for Ocean Color Science. In I. Cetinić, C. R. McClain & P. J. Werdell (Eds.), *PACE Technical Report Series, Volume 6: Data Product Requirements and Error Budgets (NASA/TM-2018 – 2018-219027/ Vol. 6)* (Vol. 6). Goddard Space Flight Space Center Greenbelt, MD: NASA

3.2.   Proxy Data Source

The Sea-viewing Wide Field-of-view Sensor (SeaWiFS, [*McClain et al.*, 2004]) provides the representative TOA radiance data for this analysis. SeaWiFS provides a good proxy for this analysis, as its 8 spectral bands span the most critical spectral range required for ocean color retrieval from OCI (400-900nm), and it provides a similar range of viewing and solar radiant path geometries as that expected from the tilting OCI sensor. A complete 4-day period of global SeaWiFS observations is utilized in this analysis (12-15 July 2003) to provide a realistic and comprehensive sampling of observational geometries and atmospheric and oceanic optical properties that influence the propagation of noise through the AC algorithm. With this observational sampling we are able to make a robust assessment of not just the performance of a typical observation, but rather over what geographic distribution or percentage of global observations we can expect to meet a specified retrieval uncertainty, for a given radiometric noise model.

3.3.   Atmospheric Correction Algorithm

The NASA standard AC algorithm is employed for the $\rho_w(\lambda)$ retrieval (NASA/TM–2016-217551), as currently implemented in the NASA l2gen software, OBPG CM version 9.1.0-5cc68e4. This algorithm, which has been adapted as a viable at-launch algorithm for the PACE OCI instrument [*Ibrahim et al.*, 2016; *Ibrahim et al.*, 2018], is based on the work of *Gordon and Wang* [1994] that uses a pair of wavelengths in the near-infrared (NIR) and a set of aerosol models [*Ahmad et al.*, 2010] to determine the aerosol scattering contribution to observed radiance and to extrapolate and subtract that contribution from the radiances observed in the visible bands (i.e., 412, 443, 490, 555, 670 nm for SeaWiFS). Noise in the NIR channels (765nm and 865nm for SeaWiFS) thus has a direct impact on uncertainty in $\rho_w(\lambda)$ retrievals at all wavelengths, which adds to the uncertainty due to noise in the bands themselves. In turbid or highly productive waters, the AC algorithm makes use of an iterative modeling approach [*Bailey et al.*, 2010] to estimate water-leaving radiance contributions in the NIR that enables the separation of aerosol signals from non-negligible water-leaving signals, but this model also allows noise in the 670nm band to influence retrieval uncertainties in all bands. In addition, the 443, 510, and 555nm channels can influence uncertainty in all bands through the corrections for spectral out-of-band effects [*Franz et al.*, 2003; *Wang and Bailey*, 2001] and bi-directional effects [*Morel et al.*, 2002].

3.4.   Instrument Noise Model

To run the MCA, we require to know the SNR at any observed signal level $L(\lambda_i)$ for each spectral band λ_i, $SNR(\lambda_i, L(\lambda_i))$. Given an observed radiance at sensor, $L(\lambda_i) = Lt(\lambda_i)$, the instrument radiometric noise, $\sigma(\lambda_i, Lt(\lambda_i))$, can then be readily computed as in Eq. 3.1. This $\sigma(\lambda_i, Lt(\lambda_i))$ represents the width of the distribution of radiometric errors that would be expected if repeated measurements were made of a source for which the true radiance is $Lt(\lambda_i)$. It provides an estimate of the measurement precision of the instrument, where the random radiometric errors are assumed to take the form of a Gaussian distribution with standard deviation $\sigma(\lambda_i, Lt(\lambda_i))$. These radiometric errors are assumed to be spectrally and spatially uncorrelated.

$$\sigma(\lambda_i, L(\lambda_i)) = \frac{L(\lambda_i)}{SNR(\lambda_i, L(\lambda_i))} \qquad \text{(Eq. 3.1)}$$

Prior to instrument design and component performance testing, we do not have complete knowledge of the expected OCI SNR at all expected signal levels. Rather, the SNR performance requirement for a

given spectral band, λ_i, is specified at one typical radiance, $L_{typ}(\lambda_i)$ (see *Ahmad and Meister* [2018] for typical ocean radiances assumed here).To first order, this can be extrapolated to other radiance levels by assuming SNR varies as the square root of the signal. Alternatively, we use the functional shape of the SeaWiFS SNR model, but scale it to match the assumed OCI SNR at the specified $L_{typ}(\lambda_i)$, Eq. 3.2.

$$SNR_{OCI}(\lambda_i, L(\lambda_i)) = SNR_{SeaWiFS}(\lambda_i, L(\lambda_i)) \frac{SNR_{OCI}(\lambda_i, L_{typ}(\lambda_i))}{SNR_{SeaWiFS}(\lambda_i, L_{typ}(\lambda_i))} \qquad \text{(Eq 3.2)}$$

The SeaWiFS signal to noise ratio (SNR) at various radiance levels, $L(\lambda_i)$, was measured at each of the eight spectral bands, λ_i, during prelaunch laboratory testing, as tabulated in Barnes [*Barnes et al.*, 1994]et al. (1994). These measurements were fit to the polynomial form of Eq. 3.1, with fitting coefficients as provided in Table 3.1 and $L(\lambda_i)$ in units of mW cm^{-2} um^{-1} sr^{-1}. Given an observed radiance at sensor, $L(\lambda_i) = Lt(\lambda_i)$, the instrument radiometric noise, $\sigma(\lambda_i, Lt(\lambda_i))$, can then be readily computed as in Eq. 3.3 and plotted in Fig. 3.1.

$$SNR_{SeaWiFS}(\lambda_i, L(\lambda_i)) = \sum_{j=0}^{4} a_j [L(\lambda_i)]^j \qquad \text{(Eq 3.3)}$$

Table 3.1. Polynomial coefficients of the SeaWiFS SNR model

| λ (nm)	a4	a3	a2	a1	a0
412	-8.2873E-03	3.8543E-01	-9.1078E+00	1.6588E+02	4.5435E-01
443	-1.2187E-02	5.2158E-01	-1.1457E+01	1.9651E+02	4.1892E-01
490	-2.9907E-02	1.0523E+00	-1.9059E+01	2.6634E+02	6.6719E-01
510	-5.6894E-02	1.6795E+00	-2.5692E+01	3.0583E+02	9.3447E-01
555	-1.3164E-01	3.0962E+00	-3.7347E+01	3.5239E+02	3.5411E-01
670	-8.6546E-01	1.1886E+01	-8.3777E+01	4.6450E+02	4.1463E-02
765	-4.9683E+00	4.5024E+01	-2.1043E+02	7.7586E+02	5.1889E-02
865	-1.3049E+01	9.3541E+01	-3.4099E+02	9.4341E+02	7.8496E-01
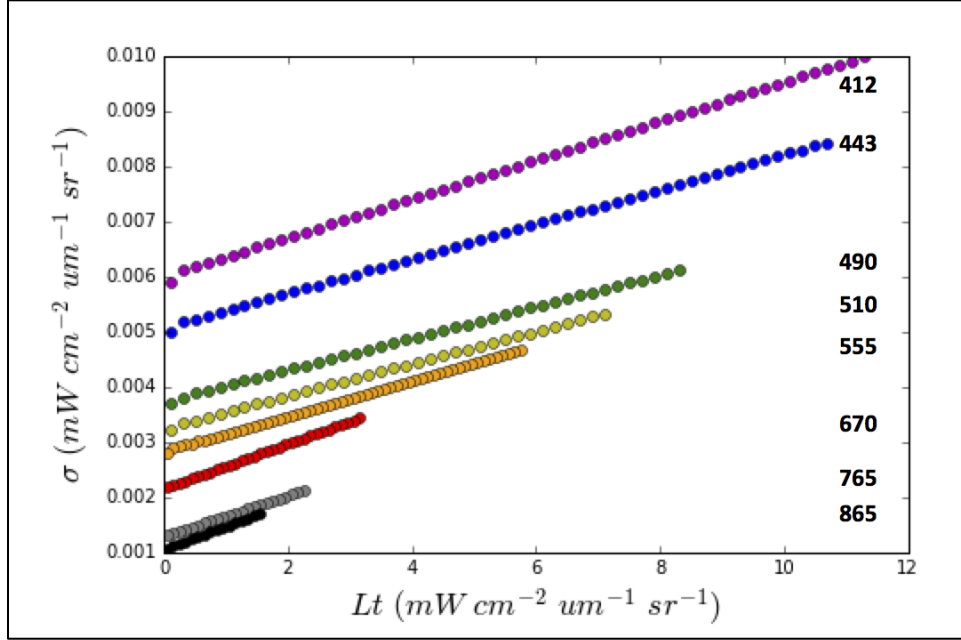
Figure 3.1. SeaWiFS instrument noise as a function of signal level for the eight spectral bands, based on prelaunch laboratory measurements (Barnes et al. 1994).

3.5.   Monte Carlo Analysis

Our goal is to estimate uncertainty in the retrieval of $\rho_w(\lambda_i)$ that results from the propagation of $\sigma\big(\lambda_i, Lt(\lambda_i)\big)$, for all λ_i, through the AC algorithm. To that end, a Monte Carlo Analysis is performed on each SeaWiFS observation (Fig. 3.2), wherein the retrieval from TOA radiances to $\rho_w(\lambda_i)$ is repeated 1000 times, but in each iteration the eight SeaWiFS radiances, $Lt(\lambda_i)$, are individually perturbed by a random sampling of the band-specific $\sigma\big(\lambda_i, Lt(\lambda_i)\big)$. Uncertainty in $\rho_w(\lambda_i)$ is then estimated as the standard deviation of the 1000 perturbed $\rho_w(\lambda_i)$ retrievals in each band. This derived uncertainty can be interpreted as the random error or precision of the $\rho_w(\lambda_i)$ retrieval due to instrument noise, and does not consider systematic biases such as absolute calibration errors or algorithm model errors. This precision will vary from observation to observation, depending on the specific atmospheric and oceanic conditions and the combined solar illumination and sensor viewing geometries.

3.6.   Analysis Example

To inform the sensor design process, a number of derived or modeled SNR scenarios for OCI have been tested using this MCA approach, with the goal to assess the resulting random error in $\rho_w(\lambda_i)$ relative to the threshold and baseline science requirements. Each tested scenario features a specific set of SNRs at specified L_{typ} for the aggregated spectral bands defined in the OCI ocean color science product requirement. As an example, the NASA PACE Science Definition Team (SDT) provided a set of derived SNRs that they estimated would satisfy the mission science requirements, wherein all visible band SNRs were uniformly set to 1000 and the NIR SNRs (700-900nm) were set to 600 [Science Definition *Team*, 2018]. An analysis of this SDT-derived SNR scenario is presented here for illustration, i.e. the values of SNR and $L_{typ}(\lambda_i)$ specified in *Science Definition Team* [2018] are used as the $SNR_{oci}(\lambda_i, L_{typ}(\lambda_i))$ inputs to Eq. 3.2.
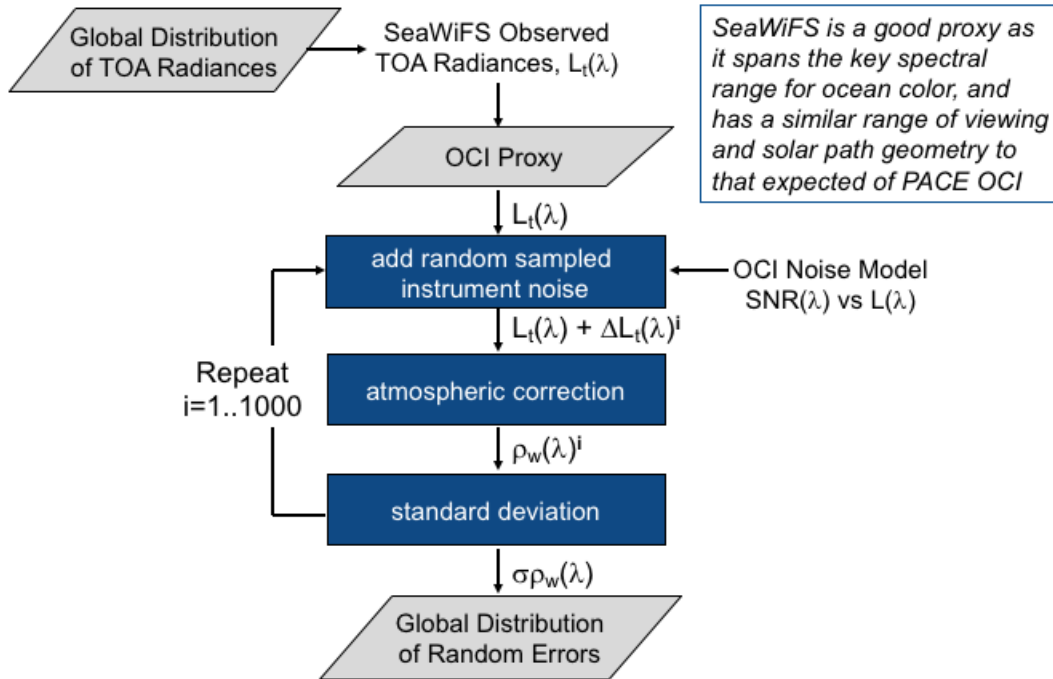
Figure 3.2. Monte Carlo analysis for a given instrument signal-to-noise (SNR) profile.

In Fig. 3.3, the MCA results for this example are presented as mapped global images showing the random error in $\rho_w(\lambda_i)$ for two spectral bands at 412 and 510nm. These images demonstrate the geographic variability in random error that can be expected, due to the interaction between the instrument noise and atmospheric correction algorithm and driven by variations in viewing and solar radiant path geometry, atmospheric conditions, and water optical properties. This variation in random error is captured as a set of frequency distributions, shown in Fig. 3.4 for four key ocean color bands. The science requirement on random error in $\rho_w(\lambda_i)$ for these four spectral bands was specified in *Science Definition Team* [2018] as 1e-3, which is indicated by the darker gray shading in Fig. 3.4. The results show that, while almost all derived errors are within this requirement, there is some small percentage of cases (pixels of Fig. 3.3, especially at 412nm) for which the threshold is exceeded. This is to be expected, as some pixels represent extreme conditions that form long tails on the frequency distribution. To capture this sensitivity, we calculate the random error that is met in each spectral band for different fractions of the global ocean: 95%, 90%, 80%, 70%, and 50%, as presented in Fig. 3.5. For this SNR scenario and specified science requirement, we show that the instrument performance is sufficient to meet the SDT-specified science requirement for 95% of the global ocean over the spectral range of greatest interest for ocean color (400-700nm).
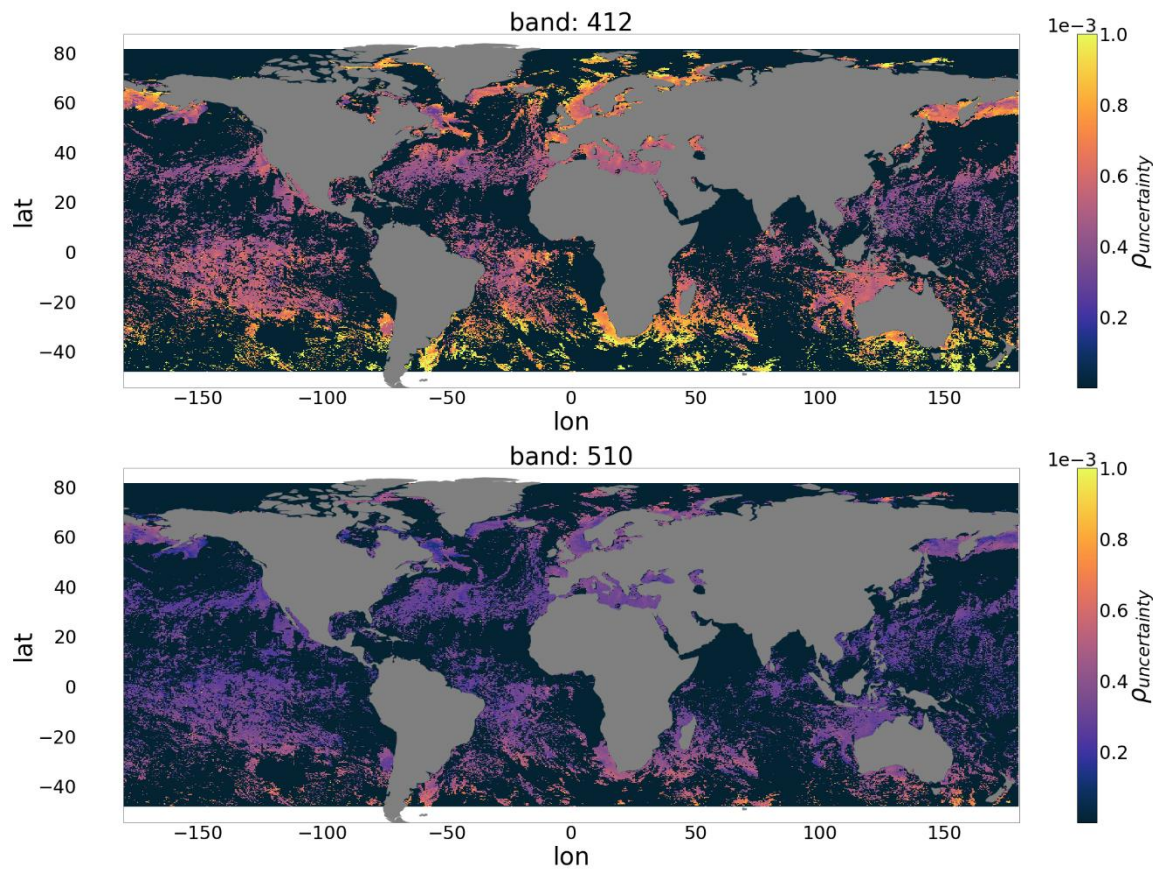
Figure 3.3. Geographic distribution of random error in $\rho_w(\lambda)$ retrievals due to propagated instrument noise representing the SDT SNR scenario, for two spectral bands at 412 and 510nm.
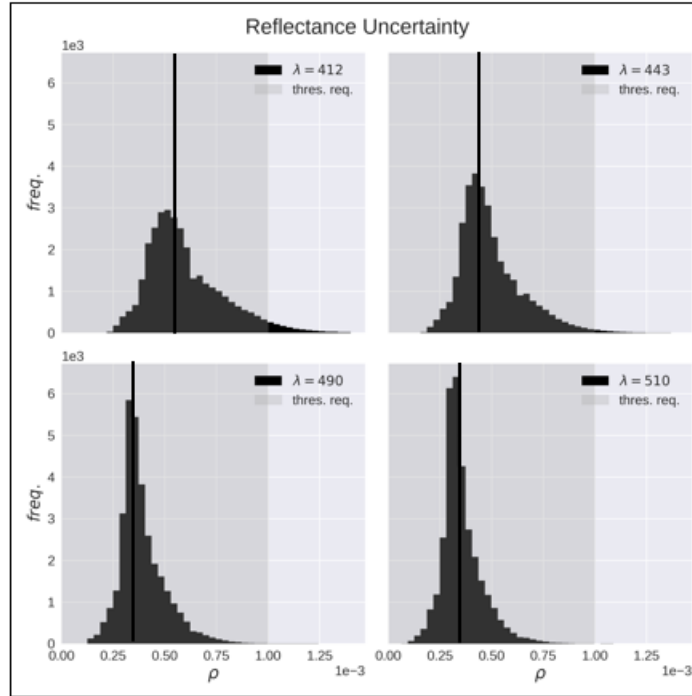
Figure 3.4. Frequency distribution of random error in $\rho_w(\lambda)$ retrievals due to instrument noise, for bands at 412, 443, 490, and 510nm, for the SDT SNR scenario. Histograms are normalized. Dark gray shade corresponds to the threshold random error requirement for the PACE mission.

Figure 3.5. Percentiles of random error in $\rho_w(\lambda)$ for the SDT SNR analysis (color lines) and their position respective to the prescribed threshold (darker gray region) of 1e-3 for bands ranging 412-555 and 5e-4 for 670. Gold region shows desired random error level for fluorescence estimation; attained less than 50% of the time with this scenario.

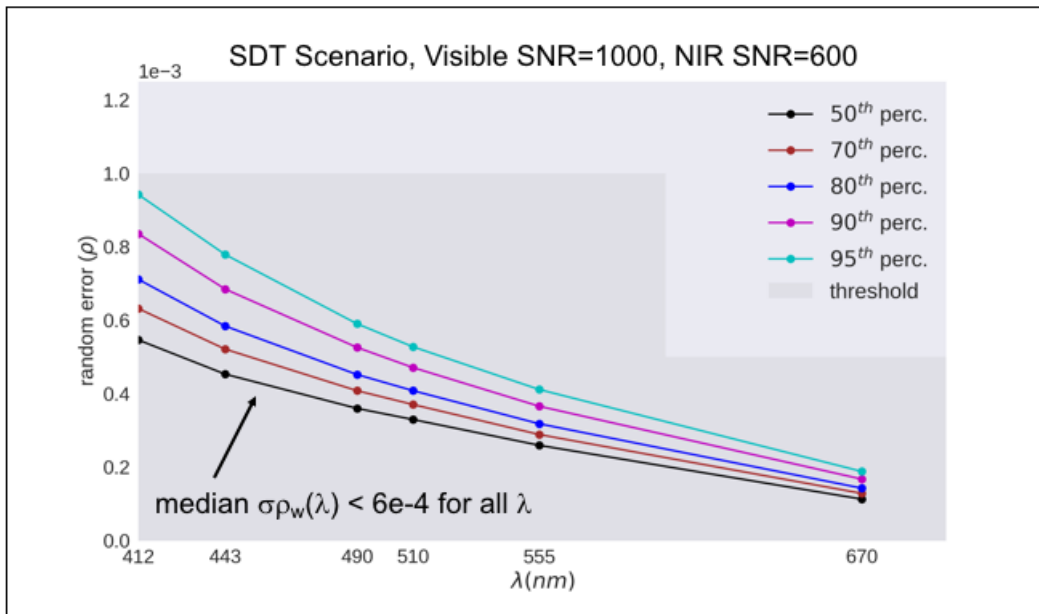## 3.7.   Verification of Modeling Approach

The atmospheric correction algorithm employed in this analysis, and the specific software implementation of that algorithm, is well documented [*Mobley et al.*, 2016] and rigorously validated [e.g. *Bailey and Werdell*, 2006], as it has been in operational use for over 20 years. The source code is in the public domain, and effectively in continuous peer review by the international ocean color community. It is the standard software employed for all NASA ocean color missions, and it has been adapted as a viable at-launch algorithm for PACE OCI.

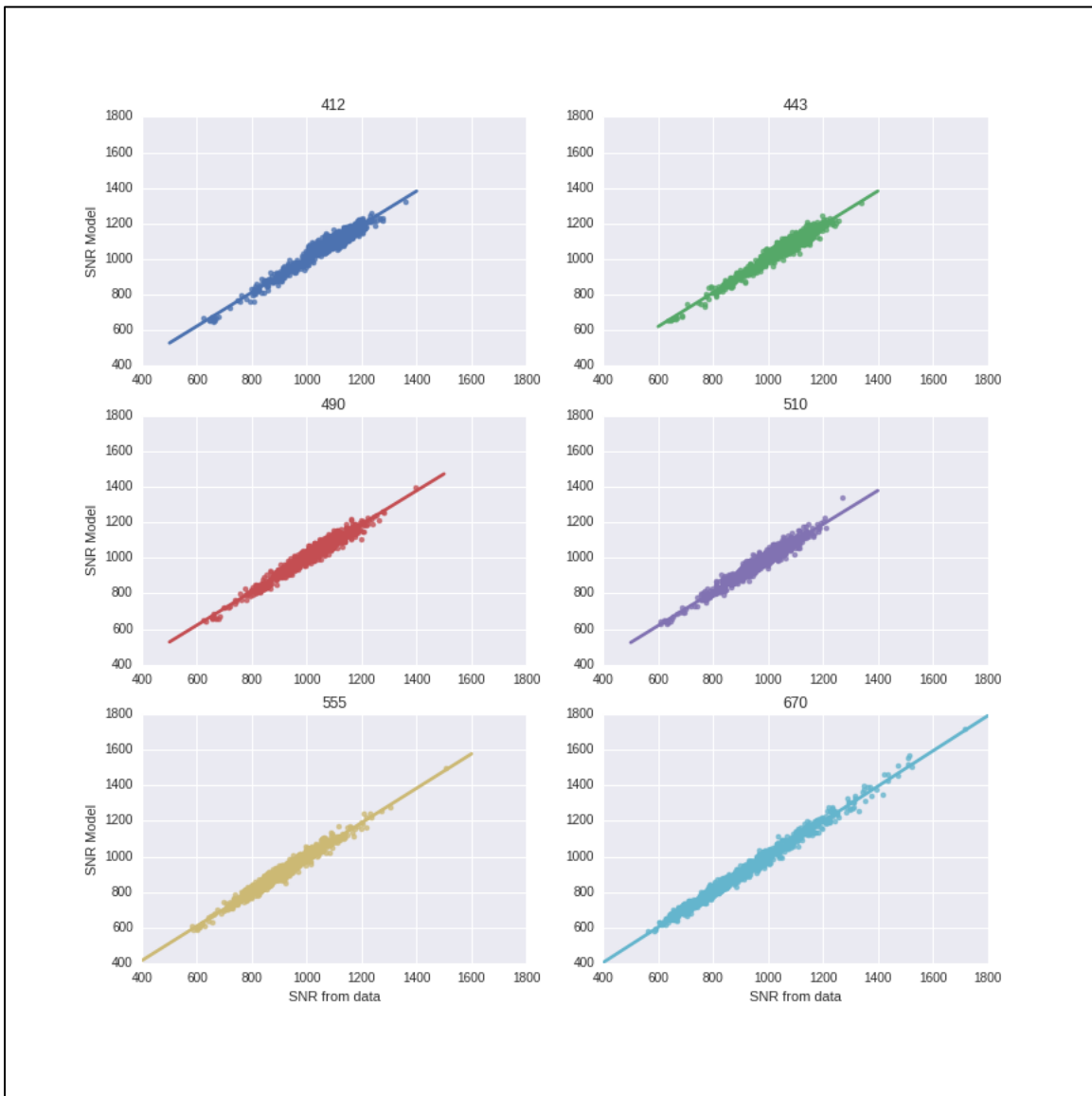*Figure 3.6. Verification of SNR model implementation within processing code. Plots show comparison of SNR from model at the observed radiances with SNR inferred from observed radiances that have been modulated by sensor noise.*

To verify that the MCA simulations are reproducing the noise model described in Section 3.2, we used results of one simulation to directly estimate simulated SNR for each band (i.e., we computed the

standard deviation of the 1000 perturbed TOA radiances in each pixel, relative to the mean signal). A comparison of this inferred SNR output with the expected SNR from the model is shown in Fig. 3.6.

3.8. Determining OCI SNR Performance Requirements

The PACE OCI random error requirement on water-leaving radiance has been allocated (Table 3.2) and defined as the error that must be met for 50% of the global ocean (black line in Fig. 3.5). This MCA serves as the primary metric for assessing whether a given SNR performance will meet the science requirement on random error in $\rho_w(\lambda_i)$. Given unlimited resources, it is conceivable that this tool could be used to find the minimum SNR performance requirement in each band to meet a given science requirement (e.g., by running a systematic series of SNR scenarios);The single scenario presented here, however, requires the equivalent of processing 4000 days of global SeaWiFS data, which currently requires 3-4 days of continuous processing on the high-performance distributed processing system of NASA's Ocean Biology Processing Group (PACE Science Data Segment). Further, the SNR in every band can affect the random error in any given band, so the number of perturbations that would have to be assessed is very large.

Table 3.2. Baseline Science Requirement and Estimated Random Error in $\rho_w(\lambda)$

λ (nm)	Random Error	Science Requirement
412	0.00052	0.0006
443	0.00045	0.0006
490	0.00036	0.0006
510	0.00034	0.0006
555	0.00027	0.0006
670	0.00012	0.0003

Alternatively, we start from an informed estimate of the SNR requirement [*Science Definition Team*, 2018] and adjust as needed to account for advancing knowledge of what is possible as the OCI design and performance capabilities evolve. For example, the NIR channels have a very large impact on the random error in the visible bands, due to the nature of the atmospheric correction algorithm, but a 600 SNR performance requirement is challenging for the instrument to meet due to the low signal (low $L_{typ}(NIR)$), over oceans relative to L_{max} which is set to quantify cloud radiances. Lowering the SNR requirement in the NIR (e.g., to 500) will increase the random error in the blue (e.g., 412), but some of that increase can be mitigated by raising the SNR performance requirement in the blue (which is easier since $L_{typ}(blue)$ is large; the ocean/atmosphere reflects strongly in the blue).There is a limit, however, to such mitigation, as further increases in SNR in a given visible band have diminishing impact on random error in that band.

Following a series of such iterations as described above, a viable profile of SNR performance requirements needed to meet baseline and threshold science requirements was established, as shown in Fig. 3.7 for ocean $L_{typ}(\lambda_i)$ [*Ahmad and Meister*, 2018]. MCA analysis of the baseline SNR performance relative to the science requirement is shown in Fig. 3.8 and Table 3.2. The results demonstrate that this predicted OCI baseline SNR performance will be sufficient to meet the allocated baseline science requirement on random error in $\rho_w(\lambda_i)$, with margin.
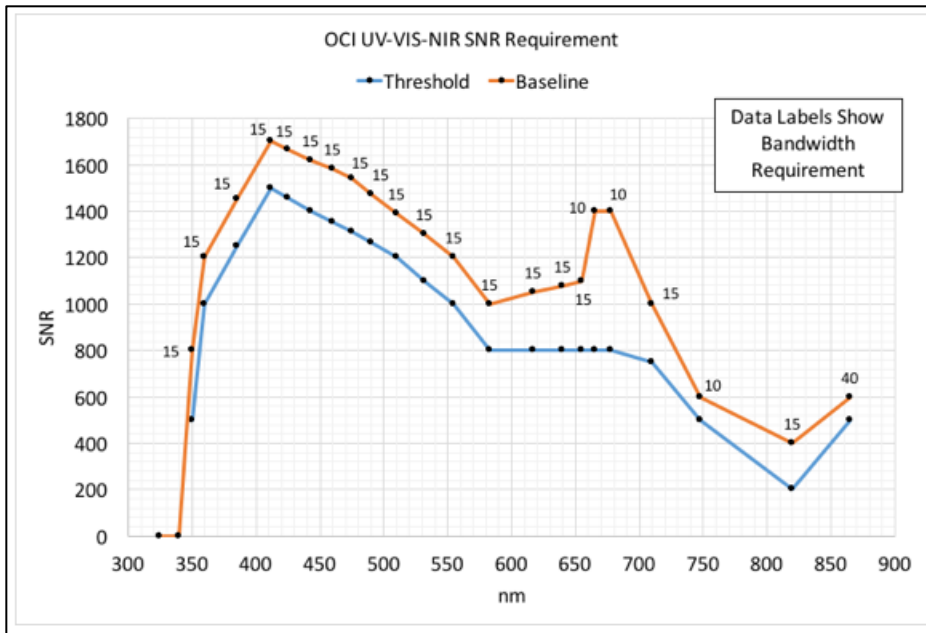
Figure 3.7. *Estimated SNR performance of the OCI instrument based on current design concept and engineering models as of June 2017.*
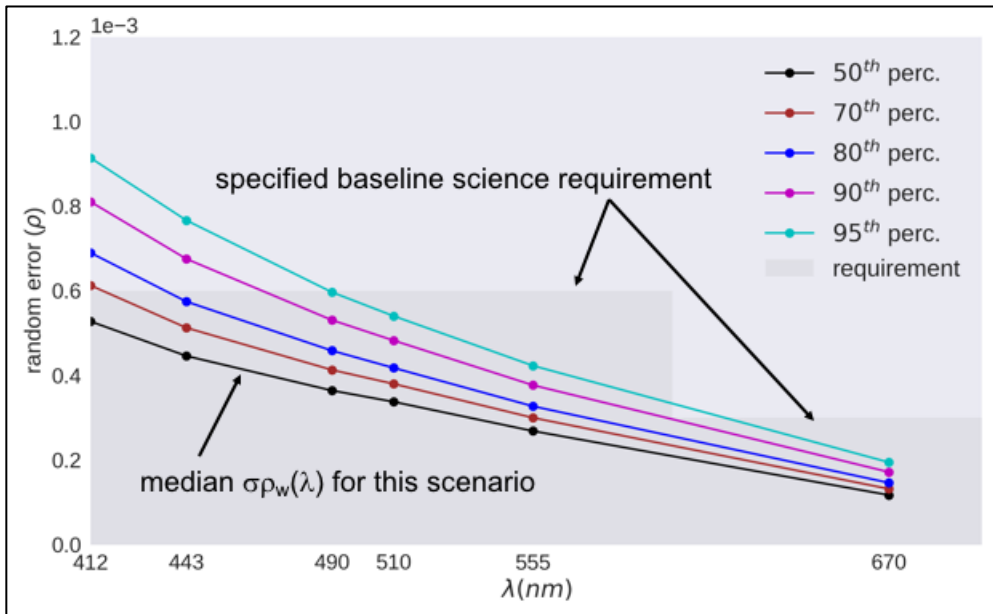
Figure 3.8. *Percentiles of random error in $\rho_w(\lambda)$ (colored lines) for the current OCI baseline SNR performance estimate of Fig. 3.6, and their position respective to the allocated baseline requirement (darker gray region).*

As the OCI design matures, and results of component noise testing are acquired, a complete SNR performance model for OCI, including margin, will be finalized. The MCA analysis will be run on that model to verify that the predicted SNR performance, considering margin, will meet the science requirement on random error in $\rho_w(\lambda_i)$. It is also anticipated that SNR performance will be measured

during OCI instrument performance testing, and the MCA analysis will be repeated again on that test data prior to launch.

3.9. Summary

A rigorous approach was developed for assessing the propagation of PACE OCI instrument noise to random error in ocean color science products. The approach utilizes the NASA standard atmospheric correction algorithm, which is a viable at-launch algorithm for OCI. The approach was used iteratively to determine a profile of instrument SNR performance requirements that meet the science requirements on $\rho_w(\lambda_i)$ allocated to allowable random error, while also considering current knowledge of engineering capabilities and limitations on the OCI preliminary design.

Chapter 4

Derivation of PACE OCI Systematic Error Approach

Frederick S. Patt, Science Applications International Corporation, Reston, Virginia [4]

Executive Summary

The Phytoplankton, Aerosol, Cloud, ocean Ecosystem (PACE) Ocean Color Instrument (OCI) radiometry will be subject to both random and systematic errors. This paper presents an overview of the systematic errors and the development of the approach for evaluating the effects of these errors on the science data products.

4.1. Introduction

The PACE Level 2 requirements [*Werdell*, 2018], specify the science data product accuracy requirements as both random and systematic errors. The random errors result from instrument noise, while the systematic errors result primarily from instrument artifacts. The overall sensor performance goals for an advanced ocean color mission, such as PACE, are defined in *Meister et al.* [2011] and *PACE Science Definition Team* [2018]. At the PACE Mission System Requirements Review (MSRR), an action was issued to develop a detailed error budget. As part of this, an approach was needed to estimate the effect of systematic sensor data errors on uncertainties in the data product accuracies. The focus of this effort was on the uncertainties in water-leaving reflectance (ρ_w) resulting from the systematic sensor data errors; it does not address errors from other sources, e.g., the atmospheric correction algorithm.

We have developed a method based on covariance analysis by *Bevington* [1969] to propagate the errors. Covariance analysis provides a rigorous basis for relating errors in one set of variables to those in another set. This method not only provides a rigorous basis for propagating the errors, but also allows for correlated errors in the input data, which may result from some instrument artifacts.

In the following sections we present a summary of the OCI artifacts, describe the approach for the covariance analysis of the systematic errors, and show sample results of the method.

4.2. Summary of OCI Artifacts

The OCI systematic error sources, known as instrument artifacts, will have a repeatable effect on the radiometric measurements, as compared to random errors that are due to instrument noise. A given measurement made under the same conditions will have the same error from the instrument artifacts, whereas the random errors will be different for every measurement.

The OCI artifacts are summarized below.

- Absolute gain – the gain that is used to convert dark-corrected counts to radiance units is measured prelaunch and adjusted using the vicarious calibration on-orbit.

- Temporal response – the time-dependent change in the instrument response is monitored using the solar diffuser and the lunar calibration.

- Temperature correction – the instrument response may vary with changes in component temperatures, including the charge-coupled devices (CCDs) and the electronics; the sensitivity to temperature is measured prelaunch.

- Response vs. scan angle (RVS) – the instrument response varies slightly as a function of the scan angle; this is measured prelaunch and monitored on-orbit using Level-2-to-3 cross-calibration analysis [*Kwiatkowska et al.*, 2008; *Meister et al.*, 2011].

- Linearity – the conversion from counts to radiance units is nominally linear over the radiance range; the deviation from linearity is measured prelaunch and possibly on-orbit using the solar diffuser; a variable sample integration-time capability has been proposed for OCI to support on-orbit linearity monitoring.

- Polarization sensitivity – the top-of-atmosphere signal is polarized by light scattering, and polarization sensitivity in the instrument affects the measured radiance; this sensitivity is measured prelaunch and monitored on-orbit using Level-2-to-3 cross-calibration analysis.

- Stray light sensitivity – the instrument sensitivity to light outside of the instantaneous field-of-view (IFOV) affects the measured radiance; this sensitivity is measured prelaunch.

- Crosstalk – there may be inter-band coupling effects in the electronics; this is measured prelaunch.

- Relative spectral response – the response of each band as a function of wavelength, including the out-of-band response, is measured prelaunch.

- Dark offset – the instrument counts at zero radiance will be measured each scan.

The combined error budget for all instrument artifacts is 0.5%.

4.3. Development of Approach

Covariance analysis is a statistical procedure for studying the relationship between errors in measurements and those in quantities derived from the measurements [*Lerner*, 1978]. In this section we describe the general approach to covariance analysis of related variables, and then the specific method developed for analysis of the OCI systematic errors.

The uncertainty of an array **x** of dimension m can be represented by the m x m covariance matrix P_x. The diagonal members of P_x represent the variances (squared uncertainties) of the values of **x**. The off-diagonal elements represent the covariance (i.e., correlations) in the uncertainties between the elements of **x**.

$$P = \begin{vmatrix} \sigma_1^2 & c_{12}\sigma_1\sigma_2 & \dots & c_{1m}\sigma_1\sigma_m \\ c_{21}\sigma_2\sigma_1 & \sigma_2^2 & \dots & c_{2m}\sigma_2\sigma_m \\ \vdots & \vdots & & \vdots \\ c_{m1}\sigma_m\sigma_1 & c_{m2}\sigma_m\sigma_2 & \dots & \sigma_m^2 \end{vmatrix} \qquad \text{(Eq. 4.1)}$$

where σ_i is the uncertainty in x_i, and c_{ij} is the correlation between the errors in x_i and x_j. Note that P is a symmetric matrix, i.e., $P_{ij} = P_{ji}$.

This expression for P is perfectly general, and does not depend on how the values of σ_i and c_{ij} are determined. For example, if the values of **x** have been computed by a state estimation process, then P can also be determined as a part of the same process [*Fallon and Rigterink*, 1978]. Alternatively, if **x** represents a set of values or measurements with known error characteristics, either from measurements or a model, then P can be computed analytically using these same characteristics. In the latter case, the errors are often assumed to be uncorrelated, and P is a diagonal matrix.

If a second array **y** of dimension n is related to the first array by a function **y** = f(**x**), then the sensitivity of the elements of **y** to changes in **x** can be represented by the n x m *Jacobian* matrix of partial derivatives:

$$
F = \begin{vmatrix}
\partial y_1/\partial x_1 & \partial y_1/\partial x_2 & \dots & \partial y_1/\partial x_m \\
\partial y_2/\partial x_1 & \partial y_2/\partial x_2 & \dots & \partial y_2/\partial x_m \\
\vdots & \vdots & & \vdots \\
\partial y_n/\partial x_m & \partial y_n/\partial x_2 & \dots & \partial y_n/\partial x_m
\end{vmatrix} \qquad \text{(Eq. 4.2)}
$$

such that for small changes in **x**:

$$f(\mathbf{x}+\delta\mathbf{x}) = f(\mathbf{x}) + F\,\delta\mathbf{x} \qquad \text{(Eq. 4.3)}$$

Like P, F is a general construct that does not presume the method for determining the partial derivatives. If f(**x**) is a differentiable function, then the partial derivatives can be computed directly. In many cases, the relationship between **x** and **y** is complex and does not allow an analytic expression for the elements of F, and in these cases the partial derivatives are computed numerically, as described below.

The covariance of the array **y**, P_y, is then related to P_x by the following transformation:

$$P_y = F\,P_x\,F^T \qquad \text{(Eq. 4.4)}$$

Let **x** represent the array of visible and NIR band top-of-atmosphere radiances ($L_t(\lambda)$), y represent the array of visible band remote sensing reflectance ($Rrs(\lambda)$), and f(**x**) represent the ocean color processing algorithms, such that $Rrs(\lambda) = f(L_t(\lambda))$. This method can be applied to determine the errors in $Rrs(\lambda)$ that will result from systematic errors in $L_t(\lambda)$ (i.e., that will result from the instrument artifacts described in Section 4.2.)

To illustrate this method, we performed an analysis of the sensitivities of $Rrs(\lambda)$ to errors in $L_t(\lambda)$ for SeaWiFS, with m = 8 (visible and NIR band L_t) and n = 6 (visible band Rrs). SeaWiFS was chosen as being representative of the current suite of multi-spectral ocean color sensors. However, the method is by no means limited to a SeaWiFS-like band set; the only requirement is that the processing algorithms (i.e., f(**x**)) be sufficiently well-defined to allow computation of the partial derivatives required for F.

The errors in the $L_t(\lambda)$ were specified as relative values (percentages) to correspond to the instrument artifact requirements. We assume for this analysis that the uncertainties in the $L_t(\lambda)$ are uncorrelated, and therefore the input covariance Px is a diagonal matrix. This assumption can easily be changed to incorporate correlations among the L_t.

In order to generate the Jacobian matrix, we needed to compute the partial derivatives of the $Rrs(\lambda)$ with respect to the $L_t(\lambda)$. The difficulty in calculating the values of $\partial\mathbf{y}/\partial\mathbf{x}$ is that they vary significantly as a function of $L_t(\lambda)$ and viewing geometry. We chose to calculate representative values by determining the

median of *Rrs* changes, i.e., f(**x**+δ**x**) - f(**x**), for values of *δLt* ranging from 0.1% to 1.0%, using a global data set of SeaWiFS data. The range of δLt was selected to span the expected value of the total systematic errors. The analysis was performed separately for each of the 8 SeaWiFS bands, using a fixed value of δL_t for each run of the global data set. Figure 4.1 shows a sample plot of the distribution of *δRrs* at 443 nm for a δL_t of 0.1%. We performed this analysis for the 8 input L_t and 6 output *Rrs* variables; the results for δL_t of 0.5% in all eight bands are shown in Table 4.1.
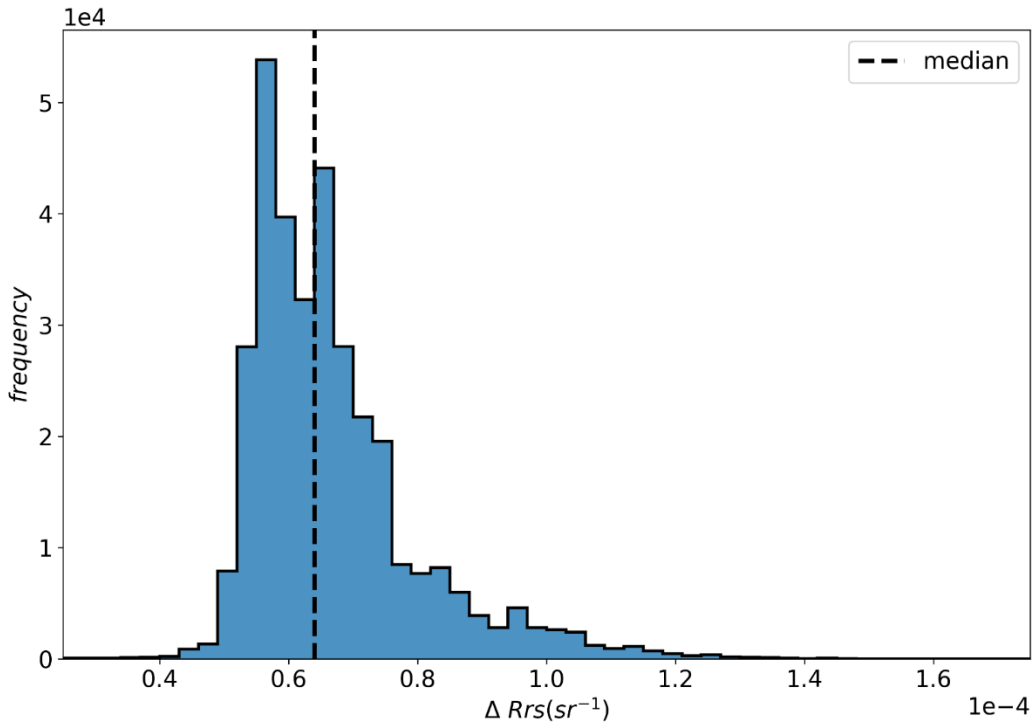
Figure 4.1. Distribution of δRrs at 443 nm for δLt at 443 nm of 0.1%, for a global SeaWiFS data set. The dashed line represents the median value of 0.63e-4.

Table 4.1. Median δRrs(λ) for δLt(λ) = 0.5%

	δLt412	*δLt443*	*δLt490*	*δLt510*	*δLt555*	*δLt670*	*δLt765*	*δLt865*
δRrs412	4.32e-4	4.e-6	6.e-6	0	-1.2e-5	0	-2.9e-4	1.88e-4
δRrs443	0	3.16e-4	6.e-6	0	-1.6e-5	0	-2.5e-4	1.58e-4
δRrs490	0	4.e-6	2.08e-4	0	-1.0e05	0	-2.1e-4	1.26e-4
δRrs510	0	4.e-6	-8.e-6	1.6e-4	1.2e-5	0	-1.9e-4	1.44e-4
δRrs555	0	2.e-6	-4.e-6	0	1.2e-4	0	-1.5e-4	8.6e-5
δRrs670	0	0	-2.e-6	0	4.e-6	5.0e-5	-7.2e-5	3.0e-5

We also needed to verify the assumptions of linearity and linear independence. Linearity ensures that the errors in f(x) are proportional to δx for small errors, while linear independence ensures that the sensitivity

of the *Rrs* to errors in each element of the L_t is independent of the errors in the other elements. As stated above, we computed changes in *Rrs* for δL_t ranging from 0.1 to 1.0%, allowing us to verify linearity; all gave the same/similar partial derivatives. We verified linear independence by computing the *Rrs* changes for changes in L_t in individual wavelengths and in multiple wavelengths simultaneously; the results verified the independence of the contributions from each of the input wavelengths.

4.4.   Examples of Results

Using the partial derivatives of δRrs with respect to δL_t as described above, we computed the covariance matrix for the six *Rrs* elements using Eq. 4.4, assuming uncorrelated errors of 0.5% in the eight L_t. The results are shown in Table 4.2.

Table 4.2. Covariance Matrix for Rrs(λ) for 0.5% Uncertainties in L_t

	Rrs410	*Rrs443*	*Rrs490*	*Rrs510*	*Rrs555*	*Rrs670*
Rrs410	3.06e-7	1.04e-7	8.54e-8	7.75e-8	5.94e-8	2.65e-8
Rrs443	1.04e-7	1.88e-7	7.46e-8	6.75e-8	5.08e-8	2.27e-8
Rrs490	8.54e-8	7.46e-8	1.03e-7	5.29e-8	4.08e-8	1.83e-8
Rrs510	7.75e-8	6.75e-8	5.29e-8	7.65e-8	4.12e-8	1.75e-8
Rrs555	5.94e-8	5.08e-8	4.08e-8	4.12e-8	4.55e-8	1.42e-8
Rrs670	2.65e-8	2.27e-8	1.83e-8	1.75e-8	1.42e-8	8.6e-9

Note that the *Rrs* off-diagonal covariance terms are significant, indicating error correlations among the bands, even though the L_t errors are assumed to uncorrelated. For example, the errors for *Rrs(555)* and *Rrs(670)* are 72% correlated. Although the Rrs correlations are not used in this calculation, they can be used to propagate the errors in *Rrs(λ)* to derived parameters.

For each value of $\delta L_t(\lambda)$ we computed the values of $\delta Rrs(\lambda)$ for the six visible bands as the square roots of the diagonal terms of the covariance matrix, and converted them to $\delta\rho_w$. The results are shown in Table 4.3 for errors in L_t t of 0.1%, 0.5% and 1.0% in all eight bands. As stated in Section II, the total budget for the instrument artifacts is 0.5%.

Table 4.3. Systematic Errors in ρ_w due to Instrument Artifact Errors in L_t

ρ_w *wavelength\ L_t error*	*0.1% L_t*	*0.5% L_t*	*1.0% L_t*
412 nm	0.0003561	0.0017386	0.0034233
443 nm	0.0002843	0.0013608	0.0026775
490 nm	0.0002105	0.0010059	0.0019781
510 nm	0.0001851	0.0008687	0.0016992
555 nm	0.0001450	0.0006704	0.0013167
670 nm	0.0000622	0.0002914	0.0005681

4.5.   Conclusion

We have developed a method for estimating the systematic errors in the retrieved remote-sensing reflectance resulting from instrument artifact errors in TOA radiance. This method has been demonstrated for total instrument artifact errors from 0.1% to 1%, and verifies linearity within that range, using the SeaWiFS wavelengths and algorithms as an example. It can be extended to error estimates for different and larger band sets (e.g., for OCI) when the processing algorithms have been developed, this method also determines correlations among the reflectances that can be used to propagate the errors to other derived products.

Chapter 5

Uncertainty in NASA ocean color observations and implications for derived biogeochemical properties

Lachlan I. W. McKinna, Go2Q Pty Ltd, Buderim, Australia [5]

Ivona Cetinić, GESTAR/Universities Space Research Association, Columbia, Maryland

Executive summary

This chapter describes an analytical framework developed to quantify how 0.5% uncertainties in spectral water-leaving reflectances propagate through bio-optical algorithms and into derived data products. This exercise was useful for understanding how the anticipated performance of the Plankton, Aerosol, Cloud, ocean Ecosystem (PACE) mission's Ocean Color Instrument (OCI) will impact the retrieval of biogeochemical variables of interest. In particular, the analytical framework developed here will facilitate analyses of how future changes OCI performance may impact derived ocean color products.

5.1.   Introduction

Marine variables of biogeochemical significance, such as chlorophyll-a pigment concentration (Chl), particulate organic carbon (POC), and inherent optical properties (IOPs) are routinely observed using space-borne ocean color remote sensing satellites. These observations are planned to be continued with NASA's Plankton, Aerosol, Cloud, ocean Ecosystem (PACE) mission. PACE will be a polar-orbiting, Earth observation mission that is planned to launch in 2022. The primary instrument on the PACE observatory will be the Ocean Color Instrument (OCI), a hyperspectral imaging spectroradiometer.

To ensure robust appraisal the PACE mission's data quality, it is critical to understand the impact radiometric uncertainties have on derived data products. In this study, we considered the impact radiometric uncertainties have upon a suite of current ocean color products. Using first-order error propagation theory [*Taylor*, 1997], we directly calculated uncertainties in derived ocean color products given uncertainties in spectral water-leaving reflectances, $\rho_w(\lambda)$, without taking into consideration any other sources of error. For this exercise, we evaluate recommended uncertainties of 5% in $\rho_w(\lambda)$ [*Mobley et al.*, 2016] with the note that this framework can be utilized to quantify the impact that any future changes in OCI performance will have on retrieving biogeochemical variables of interest.

5.2.   Data and methods

5.2.1. Bio-optical data products

The NASA Ocean Biology Data Archive and Active Distribution Center (OB.DAAC) distributes a number of derived marine data products in two separate data suites: (i) the standard ocean color (OC) data product suite and, (ii) the inherent optical properties (IOP) product suite. The OC suite comprises

established (legacy) ocean color data products that were developed during the Sea-Viewing Wide Field-of-View Sensor (SeaWiFS; 1997 – 2010) and Moderate Resolution Imaging Spectroradiometer (MODIS Aqua 2002 – present) missions. The IOP suite comprises spectral component absorption and backscattering coefficients derived using the default configuration of the Generalized Inherent Optical Properties (GIOP) algorithm framework [*Werdell et al.*, 2013a]. A selection of the OC suite and IOP suite products were used in this study (Table 5.1). More comprehensive detail of the bio-optical algorithms used to derive these data products and their associated uncertainties are detailed in Appendices A-E.

Table 5.1. Bio-optical ocean color data products

| Product name	Product suite	Symbol	Units	Reference
Chlorophyll-a pigment concentration	OC	Chl	mg m^{-3}	[*Hu et al.* [2012]; *O'Reilly et al.* [1998]]
Diffuse attenuation coefficient at 490 nm	OC	K_d(490)	m^{-1}	*Mueller* [2000]
Particulate organic carbon	OC	POC	mg m^{-3}	*Stramski et al.* [2008]
Normalized fluorescent line height	OC	nflh	mW cm^{-2} µm^{-1} sr^{-1}	*Behrenfeld et al.* [2009]
Total absorption coefficient at 443 nm	IOP	a_{tot}(443)	m^{-1}	*Werdell et al.* [2013a]
Absorption coefficient of phytoplankton at 443 nm	IOP	a_ϕ(443)	m^{-1}	*Werdell et al.* [2013a]
Absorption coefficient of colored dissolved and detrital matter at 443 nm	IOP	a_{dg}(443)	m^{-1}	*Werdell et al.* [2013a]
Particulate backscattering coefficient at 443 nm	IOP	b_{bp}(443)	m^{-1}	*Werdell et al.* [2013a]

5.2.2. Reflectance datasets
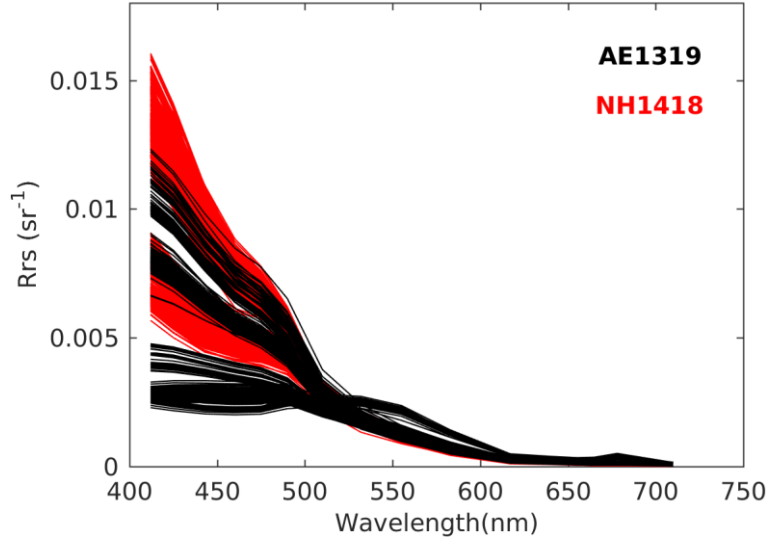
Figure 5.1. Reflectances used in this analysis. AE1319 data were collected during summer of 2013 in North Atlantic (in black), and NH1418 in summer of 2014 in Central Pacific (in red).

For the purpose of this analysis we use two field based, hyperspectral remote sensing reflectance, $R_{rs}(\lambda)$, datasets collected in the Central/North Pacific and North Atlantic Oceans, respectively [*Chase et al.*, 2017]. The data are representative of both oligotrophic and mesotrophic waters. Details of the $R_{rs}(\lambda)$ data collection methodology and processing are explained in *Chase et al.* [2017], but in short, spectra were calculated using the near-surface measurements of upwelling radiance and downwelling irradiance. $R_{rs}(\lambda)$ data were corrected for Raman scattering and angular effects. Prior to analysis, all hyperspectral $R_{rs}(\lambda)$ were spectrally sub-sampled to multispectral subset of sixteen 15 nm wide bands centered on: 412, 425, 443, 460, 475, 490, 510, 532, 555, 583, 617, 640, 655, 665, 678, 710 nm.

5.3.   Results and discussion

For the purposes of this exercise, we considered spectrally uncorrelated uncertainties in water-leaving reflectances, $\Delta\rho_w(\lambda)$, of 5%. Note, $R_{rs}(\lambda)$ is the fundamental radiometric variable used by NASA bio-optical algorithms and for a Lambertian surface is related to $\rho_w(\lambda)$ as $\rho_w(\lambda)=\pi R_{rs}(\lambda)$. For this work, input uncertainties in remote sensing reflectances, $\Delta R_{rs}(\lambda)$, that were input to bio-optical algorithms were calculated as:

$$\Delta R_{rs}(\lambda) = \frac{0.05\Delta\rho_w(\lambda)}{\rho} == 0.05\Delta R_{rs}(\lambda) \qquad \text{(Eq. 5.1)}$$

Resulting uncertainties in derived ocean color data products are given in Table 5.2 with the ranges of the retrieved parameters. A graphical representation of the distribution of derived Chl and $a_\phi(443)$ and also their relative errors is shown in Figure 5.2.

Table 5.2. Calculated uncertainties for the targeted product suite.

Product name	Symbol	Range of derived parameter	Median value of derived parameter	Median Uncertainty (%)
Chlorophyll-a pigment concentration	Chl	$3.96E\text{-}2 - 1.28$ mg m^{-3}	0.110 mg m^{-3}	10.1
Diffuse attenuation coefficient at 490 nm	Kd(490)	$2.01E\text{-}2 - 0.131$ m^{-1}	$2.91E\text{-}2$ m^{-1}	8.91
Particulate organic carbon	POC	$18.8 - 203.4$ mg m^{-3}	33.1 mg m^{-3}	7.31
Normalized fluorescent line height	nflh	$2.05E\text{-}6 - 2.73E\text{-}2$ mW cm^{-2} µm^{-1} sr^{-1}	$2.19E\text{-}3$ mW cm^{-2} µm^{-1} sr^{-1}	42.1
	$a_{tot}(443)$	$9.42E\text{-}3 - 0.127$m^{-1}	0.0185 m^{-1}	9.41
	$a_{\varphi}(443)$	$5.86E\text{-}3 - 9.45E\text{-}2$ m^{-1}	$9.63E\text{-}3$ m^{-1}	12.6
Inherent Optical Properties (IOPs)	$a_{dg}(443)$	$3.51E\text{-}3 - 3.70E\text{-}2$ m^{-1}	$8.73E\text{-}3$ m^{-1}	17.3
	$b_{bp}(443)$	$4.16E\text{-}4 - 4.01E\text{-}3$m^{-1}	$1.00E\text{-}3$m^{-1}	16.0

During this analysis we have discovered other potential utilities of this approach:

a) In complex algorithms such as the GIOP [*Werdell et al.*, 2013a], accumulation of the uncertainty depends on the parameterization within. We found that uncertainties in chlorophyll-specific absorption of phytoplankton (a_{ph}*, whose spectral shape is based on the empirical Chl derivation) are lower when Chl is derived using the line height (CI) approach than band ratio approach.

b) Most OC suite algorithms, often referred to "band ratio-type", rely on the sensitivity ratio of blue/green reflectance bands to changes biogeochemical parameters such as Chl, $K_d(490)$, and POC. More recently, however, IOP-based algorithms have been developed to drive biogeochemical parameters a function of IOPs. It is expected that IOP-based methods may have lower cumulative uncertainty on final estimates of derived data products. The analytical tools developed here provide basis for comprehensively comparing how uncertainties accumulate in band ratio-type algorithms relative to IOP-based methods. This approach will be particularly useful when using more realistic spectrally-correlated absolute radiometric errors that have a spectral shape to them (see *Franz and Karaköylü* [2018]).

c) Band ratio-type algorithms have typically utilized a small subset of spectral shortwave bands. This limitation was imposed by the multi-spectral nature of the contemporary ocean observing instruments. For a sensor with contiguous spectral bands such as OCI, the choice of blue/green bands for band ratio-type algorithms is expanded. We propose that the error propagation exercise outlined here may be used to find an optimal set of green/blue bands that minimize the error accumulation in the biogeochemical parameters (similar as above, assuming radiometric errors having a spectral shape).
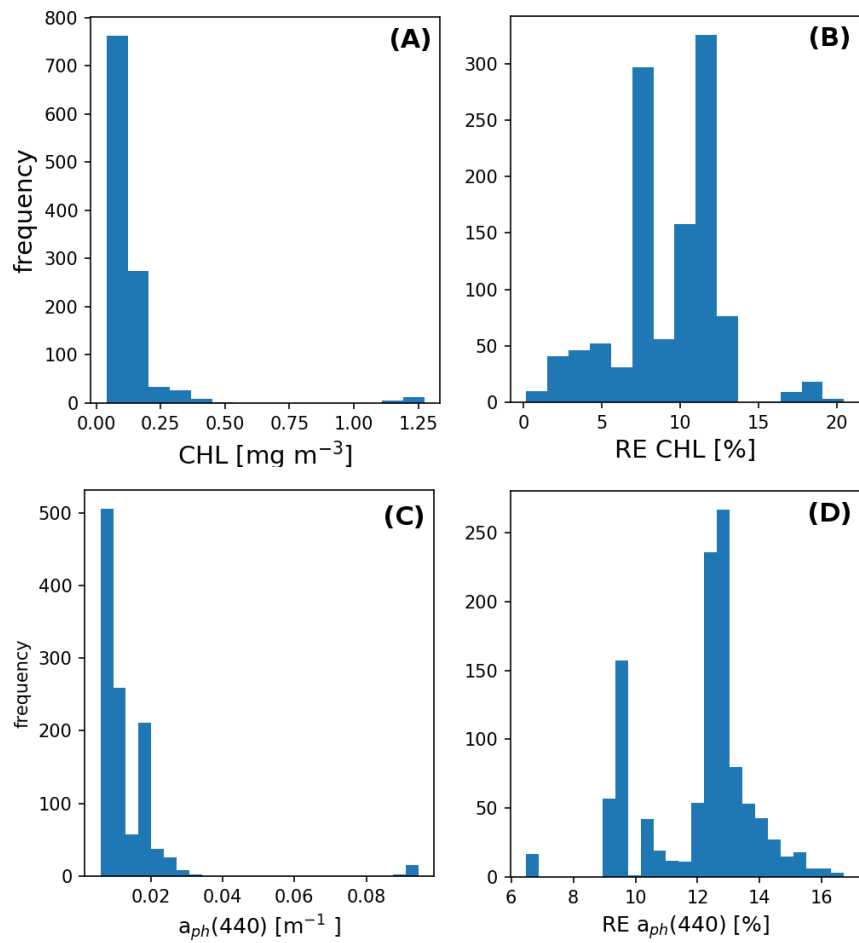
Figure 5.2. Histograms showing the relative frequency of retrieved Chl (panel A), using the Rrs from the Figure 5.1, and associated uncertainties assuming the error of 5% in Rrs (panel B). Panels C and D, same as above but for $a_\phi(440)$ and associated uncertainties.

5.4. Appendix A: Chlorophyll concentration and uncertainty

NASA's standard chlorophyll-a pigment (Chl; mg m^{-3}) algorithm is a combination of a blue-to-green maximum band ratio algorithm (Chl$_{BR}$) [*O'Reilly et al.*, 1998] and a chlorophyll index (line height) algorithm (Chl$_{CI}$) [*Hu et al.*, 2012]. During pixel-by-pixel processing, both Chl$_{BR}$ and Chl$_{CI}$ are computed. Chl$_{BR}$ is returned as the solution when Chl$_{BR}$ > 0.2 mg m^{-3} and is computed as follows:

$$\text{Chl}_{BR} = 10^{a} \qquad\qquad \text{(Eq. 5.2)}$$

which has the derivative:

$$\frac{\partial Chl_{BR}}{\partial a} = \log(10)10^{a} \qquad\qquad \text{(Eq. 5.3)}$$

where α is a polynomial function. The order of the polynomial, $N=4$, and the coefficients a_i are sensor dependent. Specifically, α is expressed as:

$$a = \sum_{i=0}^{N} a_i \left[LR \right]^{i} \qquad\qquad \text{(Eq. 5.4)}$$

and has the derivative:

$$\frac{\partial a}{\partial LR} = \sum_{i=0}^{N} i a_i \left[LR \right]^{i-1} . \qquad\qquad \text{(Eq. 5.5)}$$

The log-ratio, *LR*, term is:

$$LR = \log_{10}\left(\frac{R_{rs}(\lambda_b)}{R_{rs}(\lambda_g)} \right) \qquad\qquad \text{(Eq. 5.6)}$$

where $R_{rs}(\lambda_b)$ and $R_{rs}(\lambda_g)$ are remote sensing reflectances centered on blue and green sensor bands, respectively.

The partial derivatives of Eq. 5.6 are:

$$\frac{\partial LR}{\partial R_{rs}(\lambda_b)} = \frac{1}{\log(10)LR} \times \frac{1}{R_{rs}(\lambda_g)} \qquad\qquad \text{(Eq. 5.7a)}$$

and

$$\frac{\partial LR}{\partial R_{rs}(\lambda_g)} = -\frac{1}{\log(10)LR} \times \frac{R_{rs}(\lambda_b)}{R_{rs}(\lambda_g)^2} . \qquad\qquad \text{(Eq. 5.7b)}$$

In this analysis, we consider the Chl$_{BR}$ formulation known as "OC4" tuned for the SeaWiFS sensor where the green reference band, λ_g, is centered on 555 nm and the blue band is selected as follows:

$$R_{rs}(\lambda_b) = \max\{R_{rs}(443), R_{rs}(490), R_{rs}(510)\} \qquad\qquad \text{(Eq. 5.8)}$$

The third order polynomial coefficients a_i were determined empirically from a comprehensive *in situ* data set of coincident Chl and $R_{rs}(\lambda)$ data *[Werdell and Bailey, 2005]*. For OC4, the coefficients a_0, a_1, a_2, a_3, a_4, have values of 0.3272, -2.9940, 2.7218, -1.2259, and -0.5683, respectively.

Under the assumption that $R_{rs}(\lambda_b)$ and $R_{rs}(\lambda_g)$ are not correlated, the uncertainty in Chl$_{BR}$ is given as:

$$DChl_{BR} = \left[+\left(\frac{\partial Chl_{BR}}{\partial R_{rs}(\lambda_b)} \right)^2 DR_{rs}(\lambda_b)^2 + \left(\frac{\partial Chl_{BR}}{\partial R_{rs}(\lambda_g)} \right)^2 DR_{rs}(\lambda_g)^2 \right]^{1/2} \qquad \text{(Eq. 5.9)}$$

where $\Delta R_{rs}(\lambda_b)$ and $\Delta R_{rs}(\lambda_g)$ are the uncertainties in $R_{rs}(\lambda_b)$ and $R_{rs}(\lambda_g)$, respectively and the partial derivatives in Eq. 5.9 are computed as:

$$\frac{\partial Chl_{BR}}{\partial R_{rs}(\lambda_b)} = \frac{\partial Chl_{BR}}{\partial a} \frac{\partial a}{\partial LR} \frac{\partial LR}{\partial R_{rs}(\lambda_b)} , \qquad \text{(Eq. 5.10a)}$$

and

$$\frac{\partial Chl_{BR}}{\partial R_{rs}(\lambda_g)} = \frac{\partial Chl_{BR}}{\partial a} \frac{\partial a}{\partial LR} \frac{\partial LR}{\partial R_{rs}(\lambda_g)} . \qquad \text{(Eq. 5.10b)}$$

Chl_{CI} is returned as the solution when $Chl_{CI} \leq 0.15$ mg m^{-3} and is computed as follows:

$$Chl_{CI} = 10^b \qquad \text{(Eq. 5.11)}$$

which has the derivative:

$$\frac{\partial Chl_{CI}}{\partial b} = \log(10)10^b \qquad \text{(Eq. 5.12)}$$

where,

$$b = -0.4909 + 191.6590 \, CI \qquad \text{(Eq. 5.13)}$$

which has the derivative:

$$\frac{\partial b}{\partial CI} = 191.6590 . \qquad \text{(Eq. 5.14)}$$

The CI term has the form:

$$CI = R_{rs}(555) - \left[R_{rs}(443) + \frac{(555 - 443)}{(670 - 443)} \left(R_{rs}(670) - R_{rs}(443) \right) \right]. \qquad \text{(Eq. 5.15)}$$

with the following partial derivatives:

$$\frac{\partial CI}{\partial R_{rs}(443)} = \frac{(555 - 443)}{(670 - 443)} - 1, \qquad \text{(Eq. 5.16a)}$$

$$\frac{\partial CI}{\partial R_{rs}(555)} = 1, \qquad \text{(Eq. 5.16b)}$$

and

$$\frac{\partial CI}{\partial R_{rs}(443)} = - \frac{(555 - 443)}{(670 - 443)} \qquad \text{(Eq. 5.16c)}$$

Under the assumption that $R_{rs}(443)$, $R_{rs}(555)$ and $R_{rs}(670)$ are uncorrelated, the uncertainty in Chl_{CI} is given as:

$$\Delta Chl_{CI} = \left[\begin{array}{l} + \left(\dfrac{\partial Chl_{CI}}{\partial R_{rs}(443)} \right)^2 \Delta R_{rs}(443)^2 + \square \\[2em] \square \left(\dfrac{\partial Chl_{BR}}{\partial R_{rs}(555)} \right)^2 \Delta R_{rs}(555)^2 + \left(\dfrac{\partial Chl_{BR}}{\partial R_{rs}(670)} \right)^2 \Delta R_{rs}(670)^2 \end{array} \right]^{1/2} . \quad \text{(Eq. 5.17)}$$

where $\Delta R_{rs}(443)$, $\Delta R_{rs}(555)$ and $\Delta R_{rs}(670)$ are the uncertainties in $R_{rs}(443)$, $R_{rs}(555)$, and $R_{rs}(670)$, respectively and the partial derivatives in Eq. 5.17 are computed as:

$$\frac{\partial Chl_{CI}}{\partial R_{rs}(443)} = \frac{\partial Chl_{CI}}{\partial b} \frac{\partial b}{\partial CI} \frac{\partial CI}{\partial R_{rs}(443)} , \quad \text{(Eq. 5.18a)}$$

$$\frac{\partial Chl_{CI}}{\partial R_{rs}(555)} = \frac{\partial Chl_{CI}}{\partial b} \frac{\partial b}{\partial CI} \frac{\partial CI}{\partial R_{rs}(555)} , \quad \text{(Eq. 5.18b)}$$

and

$$\frac{\partial Chl_{BR}}{\partial R_{rs}(670)} = \frac{\partial Chl_{BR}}{\partial a} \frac{\partial a}{\partial LR} \frac{\partial LR}{\partial R_{rs}(670)} . \quad \text{(Eq. 5.18c)}$$

For intermediate conditions where $Chl_{CI} > 0.15$ mg m-3 and $Chl_{BR} \leq 0.2$ mg m-3, Chl_{CI} and Chl_{BR} values are blended together and returned as the solution [Hu et al., 2012]. The blending is performed as follows:

$$Chl_{INT} = \left(\frac{1}{0.2 - 0.15} \right) \left(\left[Chl_{CI} - 0.15 \right] Chl_{BR} + \left[0.2 - Chl_{CI} \right] Chl_{CI} \right) . \quad \text{(Eq. 5.19)}$$

The uncertainty in Chl_{INT} is calculated as follows under the assumption that Chl_{BR} and Chl_{CI} are uncorrelated:

$$\Delta Chl_{INT} = \left[\left(\frac{\partial Chl_{INT}}{\partial Chl_{CI}} \right)^2 \Delta Chl_{CI}^2 + \left(\frac{\partial Chl_{INT}}{\partial Chl_{BR}} \right)^2 \Delta Chl_{BR}^2 \right]^{1/2} \quad \text{(Eq. 5.20)}$$

where:

$$\frac{\partial Chl_{INT}}{\partial Chl_{CI}} = \frac{0.2 - 2Chl_{CI} + Chl_{BR}}{0.2 - 0.15} \quad \text{(Eq. 5.21a)}$$

and

$$\frac{\partial Chl_{INT}}{\partial Chl_{BR}} = \frac{Chl_{CI} - 0.15}{0.2 - 0.15} . \quad \text{(Eq. 5.21b)}$$

5.5.   Appendix B: Diffuse attenuation coefficient and uncertainty

NASA's standard algorithm for the deriving diffuse attenuation coefficient at 490 nm, $K_d(490)$ (m^{-1}), is based on blue-to-green reflectance ratios [*Mueller*, 2000]. The algorithm was empirically developed using a high quality *in situ* dataset of coincident $K_d(490)$ and $R_{rs}(\lambda)$ data [*Mueller*, 2000; *Werdell and Bailey*, 2005] and is computed as follows:

$$K_d(490) = 0.0166 + 10^C \qquad \text{(Eq. 5.22)}$$

which has the derivative:

$$\frac{\partial K_d(490)}{\partial a} = \log(10)10^C \qquad \text{(Eq. 5.23)}$$

where χ is a polynomial function. The order of the polynomial, *N=4*, and the coefficients b_i are sensor dependent. Specifically, χ is expressed as:

$$C = \sum_{i=0}^{N} b_i \left[\log_{10} LR \right]^i \qquad \text{(Eq. 5.24)}$$

and has the derivative:

$$\frac{\partial C}{\partial LR} = \sum_{i=0}^{N} i b_i \left[LR \right]^{i-1} . \qquad \text{(Eq. 5.25)}$$

where log-ratio, *LR*, term is:

$$LR = \log_{10} \left(\frac{R_{rs}(\lambda_b)}{R_{rs}(\lambda_g)} \right) . \qquad \text{(Eq. 5.26)}$$

The partial derivatives of Eq. B5 are:

$$\frac{\partial LR}{\partial R_{rs}(\lambda_b)} = \frac{1}{\log(10)LR} \times \frac{1}{R_{rs}(\lambda_g)} \qquad \text{(Eq. 5.27)}$$

and

$$\frac{\partial LR}{\partial R_{rs}(\lambda_g)} = -\frac{1}{\log(10)LR} \times \frac{R_{rs}(\lambda_b)}{R_{rs}(\lambda_g)^2} . \qquad \text{(Eq. 5.28)}$$

In this study, we consider the $K_d(490)$ algorithm tuned for SeaWiFS such that λ_b is 490 nm and λ_g is 555 nm, and the third order polynomial coefficients b_0, b_1, b_2, b_3, and b_4 are -0.8515, -1.8263, 1.8714, -2.4414, and -1.0690, respectively.

Under the assumption that $R_{rs}(\lambda_b)$ and $R_{rs}(\lambda_g)$ are not correlated, the uncertainty in $K_d(490)$ is given as:

$$\Delta K_d(490) = \left[+\left(\frac{\partial K_d(490)}{\partial R_{rs}(\lambda_b)} \right)^2 \Delta R_{rs}(\lambda_b)^2 + \left(\frac{\partial K_d(490)}{\partial R_{rs}(\lambda_g)} \right)^2 \Delta R_{rs}(\lambda_g)^2 \right]^{1/2} \qquad \text{(Eq. 5.29)}$$

where $\Delta R_{rs}(\lambda_b)$ and $\Delta R_{rs}(\lambda_g)$ are the uncertainties in $R_{rs}(\lambda_b)$ and $R_{rs}(\lambda_g)$, respectively and the partial derivatives in Eq. 5.29 are computed as:

$$\frac{\partial K_d(490)}{\partial R_{rs}(\lambda_b)} = \frac{\partial K_d(490)}{\partial a} \frac{\partial b}{\partial LR} \frac{\partial LR}{\partial R_{rs}(\lambda_b)} \ , \qquad \text{(Eq. 5.30a)}$$

and

$$\frac{\partial K_d(490)}{\partial R_{rs}(\lambda_g)} = \frac{\partial K_d(490)}{\partial a} \frac{\partial a}{\partial LR} \frac{\partial LR}{\partial R_{rs}(\lambda_g)} \ . \qquad \text{(Eq. 5.30b)}$$

5.6. Appendix C: Particulate organic carbon

NASA's Particulate Organic Carbon (POC) algorithm as defined by *Stramski et al.* [2008] computes near-surface particular organic carbon concentration (mg m^{-3}) as follows:

$$POC = a_{poc} x^{b_{poc}}$$ (Eq. 5.31)

where *a* and *b* are the constants 203.2 and -1.034, respectively. Eq. 5.31 has the derivative:

$$\frac{\partial POC}{\partial x} = a_{poc} b_{poc} x^{(b_{poc}-1)} \; .$$ (Eq. 5.32)

The term *x* is a blue-green reflectance ratio:

$$x = \frac{R_{rs}(\lambda_b)}{R_{rs}(\lambda_g)}$$ (Eq. 5.33)

which has the partial derivatives:

$$\frac{\partial x}{\partial R_{rs}(\lambda_b)} = \frac{1}{R_{rs}(\lambda_g)}$$ (Eq. 5.34)

and

$$\frac{\partial x}{\partial R_{rs}(\lambda_g)} = -\frac{R_{rs}(\lambda_b)}{R_{rs}(\lambda_g)^2} \; .$$ (Eq. 5.35)

$R_{rs}(\lambda_b)$ and $R_{rs}(\lambda_g)$ are remote sensing reflectances centered on blue and green bands, respectively. For MODIS, λb and λg, are centered on 443 and 547 nm, respectively.

Under the assumption that $R_{rs}(\lambda_b)$ and $R_{rs}(\lambda_g)$ are not correlated, the uncertainty in $K_d(490)$ is given as:

$$\Delta POC = \left[+\left(\frac{\partial POC}{\partial R_{rs}(\lambda_b)}\right)^2 \Delta R_{rs}(\lambda_b)^2 + \left(\frac{\partial POC}{\partial R_{rs}(\lambda_g)}\right)^2 \Delta R_{rs}(\lambda_g)^2 \right]^{1/2}$$ (Eq. 5.36)

where $\Delta R_{rs}(\lambda_b)$ and $\Delta R_{rs}(\lambda_g)$ are the uncertainties in $R_{rs}(\lambda_b)$ and $R_{rs}(\lambda_g)$, respectively and the partial derivatives in Eq. 5.36 are computed as:

$$\frac{\partial K_d POC}{\partial R_{rs}(\lambda_b)} = \frac{\partial POC}{\partial x} \frac{\partial x}{\partial R_{rs}(\lambda_b)} \; ,$$ (Eq. 5.37a)

and

$$\frac{\partial POC}{\partial R_{rs}(\lambda_g)} = \frac{\partial POC}{\partial x} \frac{\partial x}{\partial R_{rs}(\lambda_g)} \; .$$ (Eq. 5.37b)

5.7. Appendix D: Normalized fluorescent line height

NASA's algorithm for normalized fluorescence line height, *nflh* (mW cm^{-2} µm^{-1} sr^{-1}), is a measurement of chlorophyll fluorescence emission under natural sunlight [*Behrenfeld et al.*, 2009]. The algorithm uses spectral values of normalized water leaving radiances, nLw(λ). Values of *nflh* are calculated as the difference between the observed nLw(678) and a linearly interpolated nLw(678) from two adjacent bands (nLw(667) and nLw(748). Currently, the algorithm is implemented for MODIS only as:

$$\text{nflh} = \text{nLw}(678) - \text{nLw}(667)\left(\frac{70}{81}\right) - \text{nLw}(748)\left(\frac{11}{81}\right) \qquad \text{(Eq. 5.38)}$$

We note that nLw(λ) is related to $R_{rs}(\lambda)$ as follows:

$$\text{nLw}(\lambda) = F_0(\lambda)R_{rs}(\lambda) \qquad \text{(Eq. 5.39)}$$

Where, $F_0(\lambda)$ is the spectral extraterrestrial solar irradiance [*Thuillier et al.*, 2003]

The uncertainty in *nflh* is expressed as:

$$nflh = \sqrt{\left(\frac{\partial nflh}{\partial R_{rs}(667)}\right)^2 \Delta R_{rs}(667)^2 + \cdots \atop \left(\frac{\partial nflh}{\partial R_{rs}(678)}\right)^2 \Delta R_{rs}(678)^2 \left(\frac{\partial nflh}{\partial R_{rs}(748)}\right)^2 \Delta R_{rs}(748)^2} \qquad \text{(Eq. 5.40)}$$

where $\Delta R_{rs}(667)$, $\Delta R_{rs}(678)$, and $\Delta R_{rs}(748)$ are the uncertainties in $R_{rs}(667)$, $R_{rs}(678)$, and $R_{rs}(748)$, respectively and the partial derivatives in Eq. 5.40 are:

$$\frac{\partial nflh}{\partial R_{rs}(667)} = -\left(\frac{70}{81}\right)F_0(667), \qquad \text{(Eq. 5.41a)}$$

$$\frac{\partial nflh}{\partial R_{rs}(678)} = F_0(678), \qquad \text{(Eq. 5.41b)}$$

and

$$\frac{\partial nflh}{\partial R_{rs}(748)} = -\left(\frac{11}{81}\right)F_0(748). \qquad \text{(Eq. 5.41c)}$$

5.8.   Appendix E: Inherent optical properties

5.8.1. The forward model

The Generalized Inherent Optical Properties (GIOP) is a semianalytical algorithm used to derive standard IOP data products as distributed by NASA's OB.DAAC. Comprehensive discussion of the GIOP can be found elsewhere [*Franz and Werdell*, 2010; *McKinna et al.*, 2016; *Werdell et al.*, 2013a], however, below we briefly overview the algorithm.

At the core of the GIOP is a forward reflectance model that simulates the sub-surface remote-sensing reflectance, $r_{rs}(\lambda)$, as a function of the water-column's inherent optical properties (IOPs). The default configuration of the GIOP uses the quasi-single scattering approximation of *Gordon et al.* [1988] to model the subsurface remote-sensing reflectance, $r_{rs}^{mod}(\lambda)$, as a function of IOPs:

$$r_{rrs}^{mod}(\lambda) = g_0 u(\lambda) + g_1 u(\lambda) \qquad \text{(Eq. 5.42)}$$

and

$$u(\lambda) = \frac{b_b(\lambda)}{a(\lambda) + b_b(\lambda)} \qquad \text{(Eq. 5.43)}$$

where, $a(\lambda)$ is the total absorption coefficient, $b_b(\lambda)$ is the total backscattering coefficient, and g_0 and g_1 are constants with default values of 0.0949 and 0.0794, respectively. The coefficient $a(\lambda)$ can be expressed as the sum of absorbing constituent matter present:

$$a(\lambda) = a_w(\lambda) + x_f a_f^*(\lambda) + x_{dg} a_{dg}^*(\lambda) \qquad \text{(Eq. 5.44)}$$

where, the subcomponents are water, phytoplankton and colored dissolved and detrital matter denoted by the subscripts w, ϕ, and dg, respectively. In Eq. 5.43, each non-water constituent absorption coefficient is expressed as the product of a normalized spectral absorption coefficient (a^*) and its magnitude (x). Similarly, $b_b(\lambda)$ can be expressed as:

$$b_b(\lambda) = b_{bw}(\lambda) + x_p b_{bp}^*(\lambda) \qquad \text{(Eq. 5.45)}$$

where the subcomponents of water and particulate matter are denoted by the subscripts w and p. Because pure water IOPs and the spectral shapes of other constituent matter can be parameterized at runtime, $r_{rs}^{mod}(\lambda)$ becomes a function of three free variables:

$$r_{rs}^{mod}(\lambda) = f(x_f, x_{dg}, x_p). \qquad \text{(Eq. 5.46)}$$

A mathematical solution method (default: non-linear least squares optimization) is then employed to find the optimal set of x_ϕ, x_{dg}, and x_p such that $r_{rs}^{mod}(\lambda)$ best matches the sensor-observed sub-surface remote-sensing reflectance, $r_{rs}^{obs}(\lambda)$. A "best match" is achieved once some distance metric (e.g. chi-squared) falls below a predefined threshold. We note that $r_{rs}^{obs}(\lambda)$ is computed from above-water remote sensing reflectance, $R_{rs}(\lambda)$ according to Lee et al. [*Lee et al.*, 2002]:

$$r_{rs}^{obs}(\lambda) = \frac{R_{rs}(\lambda)}{0.52 + 1.7 R_{rs}(\lambda)}.$$ (Eq. 5.47)

Importantly, the GIOP's structure can be varied at runtime to assign the forward reflectance model, the normalized shapes of the IOP subcomponents ($a_\phi^*(\lambda)$, $a_{dg}^*(\lambda)$ and $b_{bp}^*(\lambda)$), and the mathematical solution method.

5.8.2. Bio-optical models

In the GIOP, the normalized shape components $a_\phi^*(\lambda)$, $a_{dg}^*(\lambda)$ and $b_{bp}^*(\lambda)$ are parameterized on a per-pixel basis using bio-optical models. Below we briefly describe the bio-optical models used in the default configuration of the GIOP.

The spectral shape $a_\phi^*(\lambda)$ is modeled per-pixel using the approach of using the methodology of *Bricaud et al.* [1998]. Specifically, $a_\phi^*(\lambda)$ is a function of Chl as derived in 5.4 Appendix A and the spectral vectors A(λ) and E(λ):

$$a_\phi^*(\lambda) = t_0 t_1(\lambda)$$ (Eq. 5.48a)

where, the scaling coefficient is:

$$t_0 = \frac{0.055}{t(\lambda_R)}$$ (Eq. 5.48b)

and:

$$t_1(\lambda) = A(\lambda)\mathrm{Chl}^{\{E(\lambda)-1\}}$$ (Eq. 5.48c)

where, the reference wavelength, λ_R, is centered on or near 440 nm. The resulting $a_\phi^*(\lambda)$ is chlorophyll-specific, hence the scaling factor x_ϕ is chlorophyll concentration (chl_giop).

The spectral shape $a_{dg}^*(\lambda)$ is modeled using an exponential function of the form:

$$a_{dg}^*(\lambda) = \exp\left\{-S_{dg}(\lambda - \lambda_R)\right\}$$ (Eq. 5.49)

where, S_{dg} is treated as a constant with a default value of 0.0183. The normalized spectral shape has a value of 1.0 at λ_R. Accordingly, the scaling factor x_{dg} is equivalent to $a_{dg}(\lambda_0)$.

The normalized particulate backscattering coefficient, $b_{bp}^*(\lambda)$, is modeled per-pixel using a power law:

$$b_{bp}^*(\lambda) = \left(\frac{\lambda_R}{\lambda}\right)^g$$ (Eq. 5.50)

The normalized spectral shape has a value of 1.0 at λ_R. The power law exponent, g, is calculated following *Lee et al.* [2002]:

$$g = 2.0\left[1 - 1.2\exp\left\{-0.9\left(\frac{r_{rs}(\lambda_R)}{r_{rs}(55x)}\right)\right\}\right] \qquad \text{(Eq. 5.51)}$$

where $r_{rs}(55x)$ is centered on or near 550 nm.

5.8.3. Inverse solution method

The GIOP has a number of built-in inverse solution (spectral matching) solution methods that am end-user can select at runtime, these including: Levenberg-Marquardt (LM) optimization, Nelder-Mead (amoeba) optimization, and linear matrix inversion (LMI). In this study, we have chosen to use LM as it is currently the solution method used in default configuration of the GIOP for deriving NASA's distributed IOP data products.

5.8.4. Uncertainty propagation

Using the formulation of *Hoge and Lyon* [1996], the problem can be expressed a linear system of equations:

$$x_f = \frac{-\left[a_w(443) + b_{bw}(443) + x_{dg}a_{dg}^*(443) + x_p b_{bp}^*(443)\right]}{a_f^*(443)} + \frac{x_p b_{bp}^*(443) + b_{bw}(443)}{u(443)a_f^*(443)} \qquad \text{(Eq. 5.52)}$$

$$x_{dg} = \frac{-\left[a_w(443) + b_{bw}(443) + x_f a_f^*(443) + x_p b_{bp}^*(443)\right]}{a_{dg}^*(443)} + \frac{x_p b_{bp}^*(443) + b_{bw}(443)}{u(443)a_{dg}^*(443)} \qquad \text{(Eq. 5.53)}$$

$$x_p = \frac{-\left[a_w(443) + b_{bw}(443) + x_{dg}a_{dg}^*(443) + x_f a_f^*(443)\right] + b_{bw}(443)}{b_{bp}^*(443)\left[u(443) - 1\right]} \qquad \text{(Eq. 5.54)}$$

The term $u(\lambda)$ is computed following *Lee et al.* [2002] as:

$$u(\lambda) = \frac{-g_0 + \sqrt{g_0^2 + 4g_1 r_{rs}(\lambda)}}{2g_1} \qquad \text{(Eq. 5.55)}$$

where, g_0 and g_1 have the values 0.089 and 0.125, respectively.

The uncertainties Δx_ϕ, Δx_{dg}, and Δx_p (which are equivalent to $a_\phi(443)$, $a_{dg}(443)$, and $b_b(443)$) can be computed analytically as functions of the uncertainties $\Delta u(443)$, $\Delta a_\phi(443)$, $\Delta a_{dg}(443)$, and $\Delta b_b(443)$ with partial derivatives computed as (wavelength has been excluded for brevity):

$$\Delta x_f = \left[\left(\frac{\partial x_f}{\partial u}\Delta u\right)^2 + \left(\frac{\partial x_f}{\partial a_f^*}\Delta a_f^*\right)^2 + \left(\frac{\partial x_f}{\partial a_{dg}^*}\Delta a_{dg}^*\right)^2 + \left(\frac{\partial x_f}{\partial b_{bp}^*}\Delta b_{bp}^*\right)^2\right]^{0.5}, \qquad \text{(Eq. 5.56)}$$

$$Dx_{dg} = \left[\left(\frac{\partial x_{dg}}{\partial u} Du \right)^2 + \left(\frac{\partial x_{dg}}{\partial a_f^*} Da_f^* \right)^2 + \left(\frac{\partial x_{dg}}{\partial a_{dg}^*} Da_{dg}^* \right)^2 + \left(\frac{\partial x_{dg}}{\partial b_{bp}^*} Db_{bp}^* \right)^2 \right]^{0.5} , \quad \text{(Eq. 5.57)}$$

$$Dx_p = \left[\left(\frac{\partial x_p}{\partial u} Du \right)^2 + \left(\frac{\partial x_p}{\partial a_f^*} Da_f^* \right)^2 + \left(\frac{\partial x_p}{\partial a_{dg}^*} Da_{dg}^* \right)^2 + \left(\frac{\partial x_p}{\partial b_{bp}^*} Db_{bp}^* \right)^2 \right]^{0.5} . \quad \text{(Eq. 5.58)}$$

We note that analytical partial derivative expressions for terms in Equations 5.56, 5.57, and 5.58 have been excluded for brevity.

Chapter 6

Uncertainty in aerosol model characterization and its impact on ocean color retrievals

Ziauddin Ahmad, Science Applications International Corporation, Reston, Virginia

Bryan A. Franz, NASA Goddard Space Flight Center, Greenbelt, Maryland

Executive Summary

As a part of an error budget study for the PACE Ocean Color Instrument (OCI), a quantitative assessment was made for the uncertainties in aerosol model characterization and their impact on ocean color retrievals, in particular, the remote sensing reflectance (*Rrs*) just above the ocean surface. Using previously computed top-of-atmosphere (TOA) reflectances based on the current standard NASA aerosol model suite [*Ahmad et al.*, 2010], pseudo observations were created for four aerosol models characterized by Angstrom exponents (α) of 1.448, 1.202, 0.788, and 0.443, chlorophyll concentrations of 0.05, 0.3 and 5.0 mg/m^3 and relative humidity of 80%. These aerosol models served as basis for determining the errors in the ocean color retrievals. 120960 pseudo observations covering a wide range of sun-viewing angles and aerosol optical thickness were considered. The pseudo observations were processed through the multiple scattering epsilon (MSE) atmospheric correction algorithm [*Ahmad, in preparation*] using black pixel approximation, with all aerosol models with Rh=80% excluded from the atmospheric correction procedure. The retrieved spectral remote sensing *Rrs* were analyzed and statistics were generated. It was found that the mean of the percent error [$100*(Rrs_{retrieved} / \text{Rrs}_{obs} -1)$] distributions for blue and green bands were around 2-3% and the standard deviations were around about 3-4%. Also, the mean of the quantity, $\pi*\Delta Rrs$, where $\Delta Rrs=Rrs_{retrieved} -Rrs_{obs}$, decreased non-linearly with an increase in wavelength. For the 412-nm band, the $\pi*\Delta Rrs$ value was 0.00045±0.0006. The dependence of $\pi*\Delta Rrs$ on solar and sensor zenith angle was also analyzed. It was found that $\pi*\Delta Rrs$ increased with solar zenith angle, with the maximum value of ~ 0.0006 at 60º. Likewise, $\pi*\Delta Rrs$ also increased with sensor zenith angle to a maximum of ~0.0007 at 60º.

6.1.   Introduction

In satellite remote sensing of the ocean, the primary quantity of interest is the spectral distribution of radiance upwelling from beneath the ocean surface, which is related to the inherent optical properties of the water. Uncertainty in retrieving this ocean color signal is highly dependent on the atmospheric correction procedure, which removes all atmospheric contributions from the total signal reaching the satellite sensor. Although the physics of atmospheric correction is well understood, the actual correction depends on the microphysical and optical properties of the aerosols, which vary temporally as well as spatially. *Ahmad et al.* [2010] and the references therein provide a good summary of the sources of different types of aerosols that are found over the globe. They also provide details of aerosol models that

---

[6] Cite as: Ahmad, Z., and B. Franz (2018). Uncertainty in aerosol model characterization and its impact on ocean color retrievals, in *PACE Technical Report Series, Volume 6: Data Product Requirements and Error Budgets (NASA/TM-2018 – 2018-219027/ Vol. 6)*, edited by I. Cetinić, C. R. McClain and P. J. Werdell, NASA Goddard Space Flight Space Center Greenbelt, MD

are currently used by NASA to process the ocean color data from a number of ocean color sensors, including SeaWiFS, MODIS, VIIRS, and MERIS. For this study, we used the *Ahmad et al.* [2010] aerosol models and the Ahmad et al. [*in preparation*] multi-scattering epsilon [MSE] atmospheric correction algorithm to investigate the effect of uncertainty in aerosol model characterization on ocean color retrievals from satellite measurements. Below, we first give a brief description of the aerosol models, MSE algorithm, and pseudo observations used in this study. The results and conclusions follow in sections 4 and 5, respectively.

6.2.   Aerosol Models

Ahmad et al.'s aerosol models are bimodal lognormal size distributions, with a fine mode and a coarse mode, that were derived from the Aerosol Robotic Network (AERONET) observations. An analysis of the AERONET data showed that the seasonal variability in the modal radii of the distributions are related to the relative humidity (RH) in the atmosphere. These findings were incorporated into the models by making the model radii as well as refractive indices explicitly dependent on the relative humidity. *Ahmad et al.* [2010] considered eight relative humidity values (30%, 50%, 70%, 75%, 80%, 85%, 90%, and 95%), and for each relative humidity value they constructed ten distributions by varying the fine mode fraction from zero to one. In all there were 80 aerosol size distributions (8 RH x 10 fine model fractions). The *Ahmad et al.* [2010] models also assume that the coarse mode aerosols are non-absorbing and that all absorptions are entirely due to the fine mode particles. The compositions of the fine mode were varied to ensure that the new models exhibit the same spectral dependence of single scattering albedo as observed in the AERONET data. These models are currently being used in standard processing by NASA to produce ocean color data from a number of sensors, including SeaWiFS, MODIS, VIIRS, and MERIS.

6.3.   Atmospheric correction algorithm

The details of the MSE atmospheric correction algorithm can be found in Ahmad et al. [*in preparation*]. Briefly, it is based on the *Ahmad et al.* [2010] aerosol models, for which the top of atmosphere (TOA) reflectance due to aerosols can be described by three parameters: relative humidity (RH), Angstrom exponent (α), and optical thickness of the aerosols (τ) in the model atmosphere. This simple parameterization is possible because the modal radii and standard deviations of the distributions, as well as the refractive indices of the aerosol constituents, are explicitly dependent on relative humidity, and therefore the Angstrom exponent is solely dependent on the relative humidity and relative weight of the fine mode of the distribution.   In other words, for any relative humidity suite, the dependence of multiple-scattering-epsilon ($\varepsilon_\lambda = \rho_\lambda / \rho_{869}$) on ρ_{869} would look like the x-y plot shown in Fig. 6.1. Here, ρ refers to TOA aerosol reflectance and the subscript numbers refer to wavelength bands.
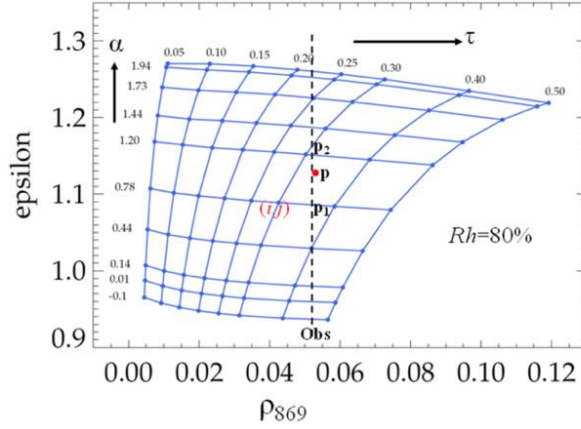
Figure. 6.1. A graph of multiple-scattering-epsilon ($\varepsilon_{748} = \rho_{748}/\rho_{869}$) versus ρ_{869} for, sza=42°, view zenith angle=30°, azimuth angle=120° and relative humidity (Rh) =80%. The solid red circle denoted by, p, represents the observation, $[(\rho_{748}/\rho_{869})_{obs}, (\rho_{869})_{obs}]$. The ρ_{869} values along the dotted vertical line are constant and are equal to $(\rho_{869})_{obs}$.

In Figure 6.1, the aerosol optical thickness (τ) varies along the 'horizontal' lines, and the Angstrom exponent (α), and extinction coefficients (C_{ext}) vary along the 'vertical' lines. The most significant feature of this graph is that it allows one to compute the reflectance at point, p, from reflectance at the closest grid point, (*i, j*), using Taylor series expansion as:

$$\rho\,(\lambda, \alpha, \tau\lambda) = \rho(\lambda, \alpha o, \tau o\lambda) + (\partial\rho/\partial\alpha)\Delta\alpha + (\partial\rho/\partial\,\tau\lambda)\Delta\tau\lambda \qquad \text{(Eq. 6.1)}$$

where, for clarity, we have dropped the arguments of ρ from the partial derivatives. The subscript ($_o$) refers to the values of α, and τ at the grid point (*i, j*). The quantities, $\Delta\alpha$ and $\Delta\tau_\lambda$ are, respectively, equal to (α-α_o) and (τ-τ_o). Note that:

$$\alpha(\varepsilon, \rho_{869}) = \alpha_o(\varepsilon_o, \rho_{o,869}) + (\partial\alpha/\partial\varepsilon)\Delta\varepsilon + (\partial\alpha\,/\partial\varepsilon)(\partial\varepsilon\,/\partial\rho)\Delta\rho_{869} \qquad \text{(Eq. 6.2)}$$

$$\tau(\lambda_{869}, \varepsilon, \rho_{869}) = \tau(\lambda_{869}, \varepsilon_o, \rho_{o,869}) + (\partial\tau/\partial\rho)\Delta\rho + (\partial\tau/\partial\rho)\,(\partial\rho/\partial\varepsilon)\Delta\varepsilon \qquad \text{(Eq. 6.3)}$$

Once, α, and τ_{869} are known, τ_λ can be determined from the following relationship:

$$\tau(\lambda,\alpha)/\,\tau(\lambda_{869},\alpha) = C_{ext}(\lambda,\alpha)/\,C_{ext}(\lambda_{869},\alpha) \qquad \text{(Eq. 6.4)}$$

where,

$$C_{ext}(\lambda,\,\alpha) = C_{ext}(\lambda,\,\alpha_o) + (\partial C_{ext}\,/\partial\alpha)\Delta\alpha \qquad \text{(Eq. 6.5)}$$

The above Equations 1-5 represent the formal solution of the atmospheric correction using the MSE method. As presented, its implementation would require computing a large number of Jacobians (sensitivity parameters) resulting in substantial increase in the size of the aerosol model look-up tables and substantial changes in the operational processing software. To circumvent this problem, the TOA reflectances were expressed as a function of aerosol optical thickness, such that τ, ρ and ε can be determined at the intersecting points of the dashed vertical line and the horizontal lines in Fig. 6.1. The procedure is described in detail in Ahmad et al. [in preparation].

6.4.   Simulation Results

For this study, pseudo observations were simulated for nine MODIS bands (412, 443, 488, 531, 547, 667, 670, 748, and 869 nm) dedicated for ocean color studies. Four bimodal aerosol models characterized by Angstrom exponents (α) of 1.448, 1.202, 0.788, and 0.443 were considered. Chlorophyll concentrations of 0.05, 0.3 and 5.0 mg/m^3 were assumed. Other details are summarized in Table 6.1.

Table 6.1. Details of the input parameters used in RT simulations of the pseudo-observations.

Parameter	Range	Tot. No
Solar Zenith Angles (θ_o)	10.0^o, --------(5°)--------75°	14
Sensor View Angle (θ)	5.0^o, -------($\sim 5^o$)--------59.2^o	12
Azimuth Angles (φ)	5.0^o, -------($\sim 5^o$)--------59.2^o	10
Aerosol Optical Thickness (τ)	0.05, 0.10, 0.15, 0.20, 0.25, 0.30	6
Chlorophyll Concentration	0.05, 0.30, 5.0	3
Aerosol Models: [Angstrom Exp (α)]	1.45, 1.21, 0.79, 0.44; $Rh = 80\%$	4
Wavelengths Bands	9 (MODIS)	9
Total No. of Observations for Each MODIS Band: (15*12*10*6*3*4)		129600

A total of 129600 pseudo observations covering a wide range of sun-viewing angles and aerosol optical thickness were generated. Note that all pseudo observations assumed an aerosol model RH of 80%. These observations were processed through the MSE atmospheric correction algorithm, with the suite of aerosol models at 80% RH excluded from the aerosol model look-up tables.

The MSE algorithm requires that, for every observation, one should select two relative humidity values from the lookup tables that bracket the RH of the observation. Since the pseudo observations were generated for RH=80%, the aerosol models for Rh=75% and 85% were used to retrieve the ocean color signal. The final results were the RH-weighted average values of the *Rrs* over the ocean.

The results are summarized in Figs. 6.2(a) through 6.2(f) as frequency distributions of errors (in percent) in the retrieved parameters (Rrs_{412}, Rrs_{443}, Rrs_{547}, Rrs_{667}, τ_{412} and α). These results show that the mean of the retrieval errors is close to zero for *Rrs* and τ and around -3.5% for α. The actual values are given in Table 6.2.

Table 6.2. Mean and standard deviation of the retrieved remote sensing reflectance (Rrs), aerosol optical thickness (τ), and Angstrom exponent (α) parameters. The subscripts refer to wavelengths in angstrom units.

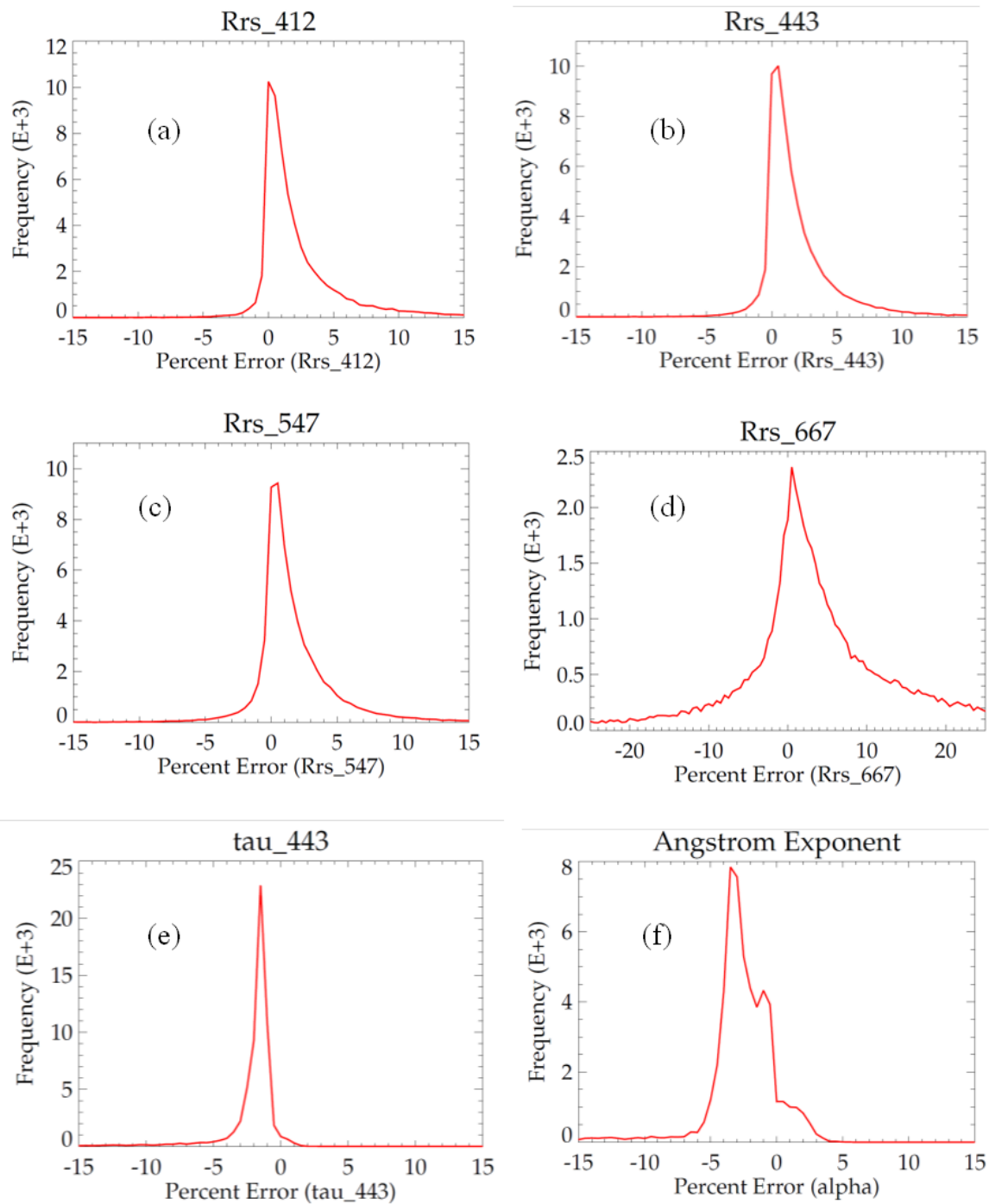|	Rrs_{412}	Rrs_{443}	Rrs_{547}	Rrs_{667}	τ_{443}	$\alpha_{(443:869)}$
Mean	2.748	2.249	2.007	5.353	-1.950	-5.117
Std. Dev	3.909	2.987	3.234	21.627	2.559	9.408

Figure 6.2. Frequency distributions of the percent error in the remote sensing reflectance (Rrs$_{412}$, Rrs$_{443}$, Rrs$_{547}$, and Rrs$_{667}$), aerosol optical thickness (τ$_{443}$), and Angstrom exponent of the retrievals from the pseudo observations.

In addition to histograms, the spectral dependence in the bias (*ΔRrs*) was also analyzed. This is shown in Fig. 6.3, where the bias, expressed as *π*ΔRrs*, is plotted against the wavelength. It shows that the bias in the *Rrs* retrieval varies non-linearly with wavelength and it is higher in blue than in green part of the spectrum.
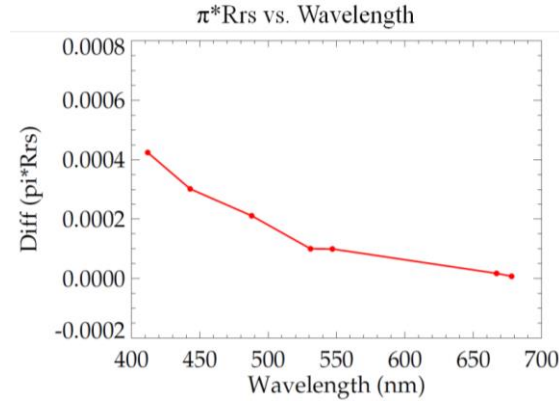

Fig 6.3. Spectral dependence in the bias of Rrs retrievals

The dependence of the bias (*ΔRrs*) on solar and sensor zenith angles were also examined. These are shown in Figs. 6.4(a) and 6.4(b) as the standard error of *ΔRrs* against solar and sensor view angles, respectively. These results show that the retrieval becomes noisier with an increase in solar and sensor view angles.
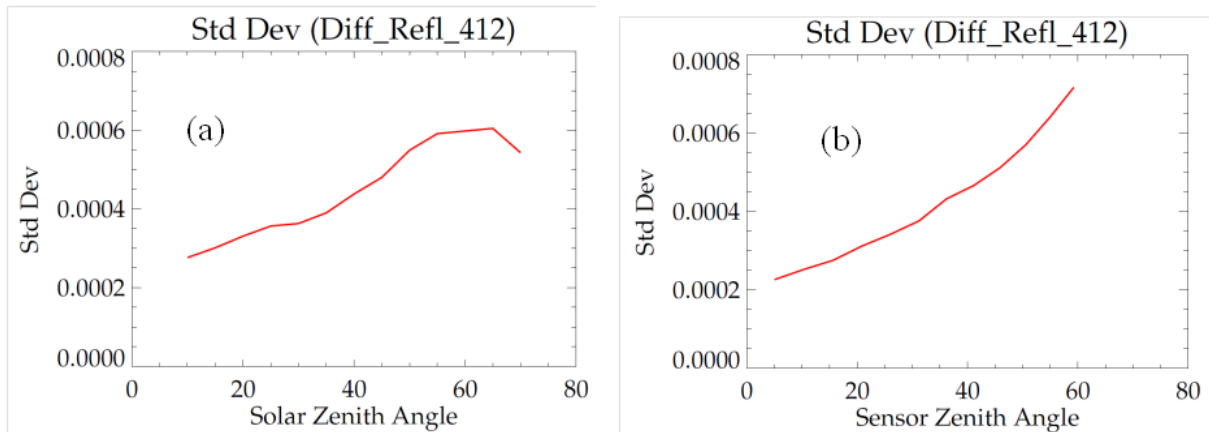

Figure 6.4. Standard deviation of the bias (ΔRrs) as function of solar zenith angle [Fig. 6.4(a)] and sensor zenith angles [Fig. 6.4(b)].

6.5.   Discussion and Conclusions

Based on the simulation results, it was found that the mean of the percent error distributions for blue and green bands were 2-3%, and the standard deviations were 3-4%. It was also found that the error in remote sensing reflectance (expressed as *π*Rrs*) decreased non-linearly with an increase in wavelength. For the 412-nm band, the mean error for the entire sample of 120960 observations was about 0.00045 ±0.006. Also, the error (*π*ΔRrs*) increased with an increase in solar as well as sensor zenith angles. The maximum value found was ~0.0006 for solar zenith angle of 60º, and ~0.0007 for sensor zenith angle of 60º.

It should be noted that these results are based on coastal and open ocean aerosol models where the relative humidity is 80%. It is recognized that the results for other relative humidity values will be slightly different. This is being analyzed and will be reported later.

Another source of error, although random, arises from the fact that the fine and coarse mode mean geometric radii (r_f, r_c) of the aerosol distributions follow the model of *Hänel* [1976], which describes the growth of the aerosol radius with relative humidity. As shown in *Ahmad et al.* [2010], the model reproduces the AERONET data; however, there is significant scatter in the data. In other words, the modal radii for fine and coarse modes could be $r_f+\Delta r_f$ and $r_c-\Delta r_c$ or $r_f-\Delta r_f$ and $r_c+\Delta r_c$ instead of r_f, r_c. Here, the subscripts, refer to fine and coarse modes of the distribution. The effect of these errors must be evaluated, particularly when reporting the error at pixel level.

Finally, for a large number of observations, the random error would decrease and the bias error will be absorbed in the vicarious calibration of the sensor, which is not addressed in this paper.

References

Ahmad, Z., and B. Franz (2018), Uncertainty in aerosol model characterization and its impact on ocean color retrievals, in *PACE Technical Report Series, Volume 6: Data Product Requirements and Error Budgets (NASA/TM-2018 – 2018-219027/ Vol. 6)*, edited by I. Cetinić, C. R. McClain and P. J. Werdell, NASA Goddard Space Flight Space Center Greenbelt, MD.

Ahmad, Z., B. A. Franz, C. R. McClain, E. J. Kwiatkowska, J. Werdell, E. P. Shettle, and B. N. Holben (2010), New aerosol models for the retrieval of aerosol optical thickness and normalized water-leaving radiances from the SeaWiFS and MODIS sensors over coastal regions and open oceans, *Appl. Opt.*, *49*(29), 5545-5560, doi:10.1364/AO.49.005545.

Ahmad, Z., and G. Meister (2018), Ltyp and Lmax calculations for PACE Ocean Color Instrument, in *PACE Technical Report Series, Volume 7: Ocean Color Instrument (OCI) Concept Design Studies (NASA/TM-2018 – 2018-219027/ Vol. 7)*, edited by I. Cetinić, C. R. McClain and P. J. Werdell, NASA Goddard Space Flight Space Center Greenbelt, MD.

Bailey, S. W., B. A. Franz, and P. J. Werdell (2010), Estimation of near-infrared water-leaving reflectance for satellite ocean color data processing, *Opt. Express*, *18*(7), 7521-7527, doi:10.1364/OE.18.007521.

Bailey, S. W., and P. J. Werdell (2006), A multi-sensor approach for the on-orbit validation of ocean color satellite data products, *Remote Sens. Environ.*, *102*(1-2), 12-23.

Barnes, R. A., W. L. Barnes, W. E. Esaias, and C. R. McClain (Eds.) (1994), *Prelaunch Acceptance Report for the SeaWiFS Radiometer. NASA Tech. Memo. 104566*, NASA Goddard Space Flight Center, Greenbelt, Maryland.

Behrenfeld, M. J., et al. (2009), Satellite-detected fluorescence reveals global physiology of ocean phytoplankton, *Biogeosciences*, *6*(5), 779-794, doi:10.5194/bg-6-779-2009.

Bevington, P. R. (1969), *Data reduction and error analysis for the physical sciences*, McGraw-Hill Book Company, New York.

Bricaud, A., A. Morel, M. Babin, K. Allali, and H. Claustre (1998), Variations of light absorption by suspended particles with the chlorophyll a concentration in oceanic (Case 1) waters : analysis and implications for bio-optical models, *J. Geophys. Res. Oceans*, *103*, 31,033 - 031,044.

Chase, A. P., E. Boss, I. Cetinić, and W. Slade (2017), Estimation of Phytoplankton Accessory Pigments From Hyperspectral Reflectance Spectra: Toward a Global Algorithm, *Journal of Geophysical Research: Oceans*, *122*(12), 9725-9743, doi:10.1002/2017JC012859.

Fallon, L., and P. V. Rigterink (1978), Introduction to Estimation Theory, in *SPacecraft Attitude Determination and Control*, edited by J. R. Wertz, D. Reidel Publishing Company, Dordrecht, Holland.

Franz, B., R. Eplee, S. Bailey, and M. Wang (2003), Changes to the atmospheric correction algorithm and retrieval of oceanic optical properties, NASA/TM-2003-206892, edited, NASA Goddard Space Flight Center, Greenbelt, Maryland.

Franz, B. A., and E. M. Karaköylü (2018), PACE OCI Signal to Noise Performance Requirement: Assessment and Verification Approach for Ocean Color Science, in *PACE Technical Report Series, Volume 6: Data Product Requirements and Error Budgets (NASA/TM-2018 – 2018-219027/ Vol. 6)*, edited by I. Cetinić, C. R. McClain and P. J. Werdell, NASA Goddard Space Flight Space Center Greenbelt, MD.

Franz, B. A., and P. J. Werdell (2010), A Generalized Framework for Modeling of Inherent Optical Propertiesin Ocean Remote Sensing Applications, *Proc. Ocean Optics XX, Anchorage, Alaska, USA, 27 September - 1 October*.

Gordon, H. R., O. B. Brown, R. H. Evans, J. W. Brown, R. C. Smith, K. S. Baker, and D. K. Clark (1988), A semianalytic radiance model of ocean color, *J. Geophys. Res. Atmos.*, *93*(D9), 10909-10924, doi:10.1029/JD093iD09p10909.

Gordon, H. R., and M. Wang (1994), Retrieval of water-leaving radiance and aerosol optical thickness over the oceans with SeaWiFS: a preliminary algorithm, *Appl. Opt.*, *33*(3), 443-452, doi:10.1364/AO.33.000443.

Hänel, G. (1976), The properties of atmospheric aerosol particles as functions of the relative humidity at thermodynamic equilibrium with the surrounding moist air, in *Advances in geophysics*, edited, pp. 73-188, Elsevier.

Hoge, F. E., and P. E. Lyon (1996), Satellite retrieval of inherent optical properties by linear matrix inversion of oceanic radiance models: An analysis of model and radiance measurement errors, *Journal of Geophysical Research: Oceans*, *101*(C7), 16631-16648, doi:10.1029/96JC01414.

Hu, C., Z. Lee, and B. Franz (2012), Chlorophyll aalgorithms for oligotrophic oceans: A novel approach based on three-band reflectance difference, *Journal of Geophysical Research: Oceans*, *117*(C1), n/a-n/a, doi:10.1029/2011JC007395.

Ibrahim, A., B. Franz, Z. Ahmad, R. Healy, and B. Gao (2016), Hyperspectral Atmospheric Correction using L2gen, paper presented at American Geophysical Union, Ocean Sciences Meeting 2016, abstract# EC34D-1208.

Ibrahim, A., B. Franz, Z. Ahmad, R. Healy, K. Knobelspiesse, B.-C. Gao, C. Proctor, and P.-W. Zhai (2018), Atmospheric correction for hyperspectral ocean color retrieval with application to the Hyperspectral Imager for the Coastal Ocean (HICO), *Remote Sens. Environ.*, *204*, 60-75, doi:https://doi.org/10.1016/j.rse.2017.10.041.

Kwiatkowska, E. J., B. A. Franz, G. Meister, C. R. McClain, and X. Xiong (2008), Cross calibration of ocean-color bands from Moderate Resolution Imaging Spectroradiometer on Terra platform, *Appl. Opt.*, *47*(36), 6796-6810.

Lee, Z., K. L. Carder, and R. A. Arnone (2002), Deriving inherent optical properties from water color: a multiband quasi-analytical algorithm for optically deep waters, *Appl. Opt.*, *41*(27), 5755-5772, doi:10.1364/AO.41.005755.

Lerner, G. M. (1978), Covariance Analysis, in *Spacecraft Attitude and Control*, edited by J. R. Wertz, D. Reidel Publishing Company, Dordrecht, Holland.

McClain, C. R., G. C. Feldman, and S. B. Hooker (2004), An overview of the SeaWiFS project and strategies for producing a climate research quality global ocean bio-optical time series, *Deep Sea Research Part II: Topical Studies in Oceanography*, *51*(1-3), 5-42.

McKinna, L. I. W., and I. Cetinić (2018), Uncertainty in NASA ocean color observations and implications for derived biogeochemical properties, in *PACE Technical Report Series, Volume 6: Data Product Requirements and Error Budgets (NASA/TM-2018 – 2018-219027/ Vol. 6)*, edited by I. Cetinić, C. R. McClain and P. J. Werdell, NASA Goddard Space Flight Space Center Greenbelt, MD.

McKinna, L. I. W., P. J. Werdell, and C. W. Proctor (2016), Implementation of an analytical Raman scattering correction for satellite ocean-color processing, *Opt. Express*, *24*(14), A1123-A1137, doi:10.1364/OE.24.0A1123.

Meister, G., C. R. McClain, Z. Ahmad, S. W. Bailey, R. A. Barnes, S. Brown, R. E. Eplee, B. Franz, A. Holmes, and W. B. Monosmith (2011), Requirements for an advanced ocean radiometer*Rep.*

Mobley, C. D., J. Werdell, B. Franz, Z. Ahmad, and S. Bailey (2016), Atmospheric Correction for Satellite Ocean Color Radiometry, A Tutorial and Documentation*Rep.*, NASA Goddard Space Flight Center, Greenbelt, MD.

Morel, A., D. Antoine, and B. Gentili (2002), Bidirectional reflectance of oceanic waters: accounting for Raman emission and varying particle scattering phase function, *Appl. Opt.*, *41*(30), 6289-6306.

Mueller, J. L. (2000), SeaWiFS algorithm for the diffuse attenuation coefficient, K(490), using water-leaving radiances at 490 and 555 nm, in *NASA Technical Memorandum 2000-206829*, edited by S. B. Hooker and E. Firestone, R, p. 51, NASA Goddard Space Flight Center, Greenbelt, USA.

Nishihama, M., R. Wolfe, D. Solomon, F. Patt, J. Blanchette, A. Fleig, and E. Masuoka (1997), MODIS level 1A Earth location: Algorithm theoretical basis document version 3.0, *SDST-092, MODIS Science Data Support Team*.

O'Reilly, J. E., S. Maritorena, B. G. Mitchell, D. A. Siegel, K. L. Carder, S. A. Garver, M. Kahru, and C. McClain (1998), Ocean color chlorophyll algorithms for SeaWiFS, *J. Geophys. Res. Oceans*, *103*(C11), 24937-24953, doi:10.1029/98JC02160.

Patt, F. (2011), SeaWiFS operational geolocation assessment system, in *Image Registration for Remote Sensing*, edited, Cambridge University Press.

Patt, F. (2018), Derivation of PACE OCI Systematic Error Approach, in *PACE Technical Report Series, Volume 6: Data Product Requirements and Error Budgets (NASA/TM-2018 – 2018-219027/ Vol. 6)*, edited by I. Cetinić, C. R. McClain and P. J. Werdell, NASA Goddard Space Flight Space Center Greenbelt, MD.

Patt, F. S., and R. E. Eplee (2018), Strategy and Requirements for the PACE OCI Lunar Calibration, in *PACE Technical Report Series, Volume 7: Ocean Color Instrument (OCI) Concept Design Studies (NASA/TM-2018 – 2018-219027/ Vol. 7)*, edited by I. Cetinić, C. R. McClain and P. J. Werdell, NASA Goddard Space Flight Space Center Greenbelt, MD.

Stramski, D., et al. (2008), Relationships between the surface concentration of particulate organic carbon and optical properties in the eastern South Pacific and eastern Atlantic Oceans, *Biogeosciences*, *5*(1), 171-201, doi:10.5194/bg-5-171-2008.

Taylor, J. R. (1997), *Introduction to Error Analysis, the Study of Uncertainties in Physical Measurements, 2nd Edition*, University of Science Books, New York.

Team, P. S. D. (2018), Pre-Aerosol, Clouds, and ocean Ecosystem (PACE) Mission Science Definition Team Report*Rep.*, NASA Goddard Space Flight Center, Greenbelt, MD.

Thuillier, G., M. Hersé, D. Labs, T. Foujols, W. Peetermans, D. Gillotay, P. C. Simon, and H. Mandel (2003), The Solar Spectral Irradiance from 200 to 2400 nm as Measured by the SOLSPEC Spectrometer from the Atlas and Eureca Missions, *Sol. Phys.*, *214*(1), 1-22.

Wang, M., and S. W. Bailey (2001), Correction of sun glint contamination on the SeaWiFS ocean and atmosphere products, *Appl. Opt.*, *40*(27), 4790-4798, doi:10.1364/AO.40.004790.

Werdell, P. J. (2018), PACE Ocean Color Science Data Product Requirements, in *PACE Technical Report Series, Volume 6: Data Product Requirements and Error Budgets (NASA/TM-2018 – 2018-219027/ Vol. 6)*, edited by I. Cetinić, C. R. McClain and P. J. Werdell, NASA Goddard Space Flight Space Center Greenbelt, MD.

Werdell, P. J., and S. W. Bailey (2005), An improved in-situ bio-optical data set for ocean color algorithm development and satellite data product validation, *Remote Sensing of Environment*, *98*(1), 122-140, doi:http://dx.doi.org/10.1016/j.rse.2005.07.001.

Werdell, P. J., B. A. Franz, S. W. Bailey, G. C. Feldman, E. Boss, V. E. Brando, M. Dowell, T. Hirata, S. J. Lavender, and Z. Lee (2013a), Generalized ocean color inversion model for retrieving marine inherent optical properties, *Appl. Opt.*, *52*(10), 2019-2037.

Werdell, P. J., B. A. Franz, J. T. Lefler, W. D. Robinson, and E. Boss (2013b), Retrieving marine inherent optical properties from satellites using temperature and salinity-dependent backscattering by seawater, *Opt Express*, *21*(26), 32611-32622, doi:10.1364/OE.21.032611.

Wolfe, R. E., M. Nishihama, J. Le Moigne, N. Netanyahu, and R. Eastman (2011), Accurate MODIS global geolocation through automated ground control image matching, in *Image Registration for Remote Sensing*, edited, Cambridge University Press.

Previous Volumes in This Series